Modeling solar cells with recombination

by

Prabhjot Kaur Guram

A THESIS SUBMITTED IN PARTIAL FULFILLMENT OF
THE REQUIREMENTS FOR THE DEGREE OF

MASTER OF APPLIED SCIENCE

in

The College of Graduate Studies

(Electrical Engineering)

THE UNIVERSITY OF BRITISH COLUMBIA

(Okanagan)

November 2011

© Prabhjot Kaur Guram 2011

Abstract

An elementary model for the analysis of a photovoltaic solar cell is proposed. This analysis is rooted in the current-voltage device characteristics associated with a p-n junction in conjunction with a model for a solar flux controlled current source; this follows the approach of Prince [M. B. Prince, *Journal of Applied Physics*, vol. 26, pp. 553-540, 1955], the p-n junction architecture being that underlying the photovoltaic solar cell. Recombination processes were modeled through two means: (1) an empirical expression for the current-voltage device characteristics with an associated ideality factor, η, whose value determines the importance of recombination processes, and (2) a more advanced expression that includes a recombination current. It is shown that the simplified empirical expression is overly simplified and that its use leads to artifacts, i.e., the suggestion that recombination processes could actually enhance the fill-factor. In contrast, the more realistic current-voltage device characteristic, which includes both ideal and recombination related current densities, suggests that recombination processes actually will reduce the fill-factor. This later observation is in accord with the experimental observation.

Table of Contents

Abstract ii

Table of Contents iii

List of Tables v

List of Figures vi

List of Symbols xiii

Glossary xix

Acknowledgements xx

1 Introduction 1

2 The solar spectrum and background material 9

2.1 Background 9

2.2 Solar cell technology developments 11

2.3 Blackbody radiation 13

2.4 The solar spectrum 25

2.5 Integrated solar spectrum 28

3 General theory of the p-n junction with recombination . . 33

3.1 Rationale 33

3.2 The geometric layout of the p-n junction 34

3.3 Drift and diffusion processes 35

3.4 The p-n junction with no applied bias 44

3.5 The p-n junction under forward-bias 54

3.6 The p-n junction under reverse bias 61

3.7 Recombination processes 61

4 Solar cell performance analysis 68

4.1 Motivation 68

4.2 Solar cell geometries 71

4.3 Photovoltaic solar cell behavior 73

4.4 Photovoltaic solar cell performance metrics 73

4.5 Photovoltaic solar cell device modeling 75

4.6 Relationship with the material properties 84

4.7 The role of the parasitic resistances on the performance of a photovoltaic solar cell 85

4.8 The solar spectrum and photovoltaic solar cell performance . 90

4.9 Recombination within solar cells 95

5 Conclusions 100

References 102

List of Tables

2.1 The integrated solar spectra obtained for the upper wavelength in Eq. (2.33) being set to ∞. This corresponds to integrating the solar spectra over the entire range of wavelengths. 31

3.1 The electron and hole drift mobilities associated with c-Si and c-Ge at 300 K [27]. 38

3.2 The electron and hole diffusion coefficients associated with c-Si and c-Ge at 300 K [28]. 41

3.3 The electron and hole diffusion lengths associated with c-Si and c-Ge at 300 K [26]. 44

List of Figures

1.1 Worldwide energy consumption by industrial societies as a function of the year. The data depicted in this plot is from the US Department of Energy [1]. 2

1.2 The efficiency of c-Si based solar cells as a function of the year. The data is taken from Hezel [17]. 6

1.3 A schematic of a p-n junction. The p-type region is abutted next to the n-type region. The neutral and space-charge regions are depicted. 8

2.1 A three dimensional electromagnetic cavity of the dimensions $L \times L \times L$. 14

2.2 Points in n-space. Each point corresponds to an allowed set of n_x, n_y, and n_z values, corresponding to a possible solution of Eq. (2.1). 15

2.3 The energy per electromagnetic mode as a function of $\frac{\hbar\omega}{kT}$. The classical result is contrasted with that due to Planck. The results are presented in a dimensionless form through a divison by the classical result, kT. 19

2.4 The energy density in an electromagnetic cavity as a function of the wavelength. The temperature is set to 5780 K for the purposes of this analysis. The classical result, i.e., Eq (2.16), is contrasted with result of Planck, i.e., the quantum result, Eq (2.24). 22

2.5 The Earth orbiting the Sun at radius r_{se}. The radius of the Sun itself is r_s. These distances have been exaggerated on this figure for the purposes of illustration. 24

2.6 The solar spectrum, i.e., the power flux spectrum received at the periphery of the Earth's atmosphere, as a function of wavelength of blackbody radiation for different temperatures. These temperatures correspond to the temperature of the surface of the Sun. Eq. (2.31) is used for the purposes of this analysis, where r_s is set to 7.0×10^5 km and r_{se} is set to 1.5×10^8 km. 26

2.7 The angle of incidence, the vertical axis, and the direction of the Sun's rays. 29

2.8 The solar spectra corresponding to the AM0 and AM1.5 cases. The experimental data is taken from NREL [24]. The blackbody solar spectrum is also depicted, for the Sun's surface temperature set to 5780 K [23]. 30

2.9 The integrated solar spectra corresponding to the AM0 and AM1.5 solar spectra. The integrated blackbody solar spectrum is also depicted for the Sun's surface temperature set to 5780 K [23]. 32

3.1 The geometric layout of a representative one-dimensional abrupt p-n junction. M denotes the metallurgical junction between the p-type and n-type regions. 36

3.2 The contributions to the overall current flux attributable to the various drift and diffusion processes. It is assumed that the electric field points from right to left [26]. The p-n junction architecture has been assumed. 42

3.3 The distribution of charges within a one dimensional abrupt p-n junction. 45

3.4 The depletion region formed in a p-n junction under no bias. The net distributed charge, ρ_{net}, is also indicated. E_0 denotes the "built-in" electric field. 47

3.5 The electric field within a p-n junction under no bias. The electric field points from right to left, $x = -W_p$ and $x = W_n$ denoting the space-charge/neutral region boundaries for the p-type and n-type regions, respectively [26]. 48

3.6 The electric field corresponding to a p-n junction under no bias. V_o denotes the "built-in" potential. 50

3.7 The energy band diagram of an unbiased p-n junction [29]. . 51

3.8 The charge carrier concentrations as a function of the position within the p-n junction. 52

3.9 The energy band diagram of a forward-biased p-n junction [29]. 55

3.10 Depletion region formed in a p-n junction under forward bias. Note that the space-charge region is narrower than for the no bias case. 56

3.11 The excess hole and electron concentrations in a p-n junction Eqs. (3.37) and (3.38) establish the boundary conditions. The $x = -W_p$ represents the location of the space-charge/neutral region boundary in the p-type region of junction. The $x = W_n$ represents the location of the space-charge/neutral region boundary in the n-type region of junction. 58

3.12 The contributions to the current density associated with the drift and diffusion processes. 59

3.13 Depletion region formed in a p-n junction under reverse bias. Note that the space-charge region is wider than for the no bias case. 62

3.14 The energy band diagram for a reverse-biased p-n junction [29]. 63

3.15 The injection of charge carriers and the recombination within the space-charge region. 64

3.16 The current density-voltage device characteristics corresponding to Eq. (3.48) with J_{so} set to 1 μA/cm^2 and J_{ro} set to 10 nA/cm^2. The temperature is set to 300 K. 66

4.1 Model for the behavior of a photovoltaic solar cell. The p-n junction is in parallel with a solar flux controlled current source. This circuit model follows the suggestion of Prince [30]. 69

4.2 A representative one dimensional p-n junction that may be used for photovoltaic device applications. Note that the p-type layer is thicker than the n-type layer. 72

4.3 A representative current-voltage device characteristic associated with a photovoltaic solar cell. 74

4.4 Representative current-voltage device characteristics associated with a photovoltaic solar cell for various fill-factor selections. 76

4.5 The open-circuit voltage, V_{oc}, scaled by the thermal voltage, $\frac{kT}{q}$, as a function of the ratio, $\frac{I_L}{I_o}$, for the ideality factor, η, set to unity. 78

4.6 The open circuit voltage, V_{oc}, as a function of photocurrent, I_L. I_o is set to 10^{-9} A for the purposes of this analysis. Two selections of η are considered. The temperature is set to 300 K for the purposes of this analysis. 80

4.7 The power delivered to an external load as a function of the applied voltage for two selections of the ideality factor, η. For the purposes of this analysis, I_o is set to 10^{-9} A and I_L is set to 100 mA. The temperature is set to 300 K for all cases. . . 81

4.8 The fill-factor as a function of the photocurrent, I_L. Two selections of η are considered. For all cases, I_o is set to 10^{-9} A and the temperature is set to 300 K. 83

4.9 The circuit model for a photovoltaic solar cell with the parasitic resistances taken into account. 86

4.10 The current-voltage device characteristic associated with a photovoltaic solar cell, as modeled in Figure 4.9, for a number of selections of the shunt resistance, R_{sh}. For all cases, I_o is set to 10^{-9} A, I_L is set to 100 mA, and the temperature is set to 300 K. This plot is determined using Eq. (4.9). The series resistance, R_s, is set to zero in all cases. 87

4.11 The current-voltage device characteristic associated with a photovoltaic solar cell, as modeled in Figure 4.9, for a number of selections of the series resistance, R_s. For all cases, I_o is set to 10^{-9} A, I_L is set to 100 mA, and the temperature is set to 300 K. It is noted that when the current is zero, all the voltages converges on the same point. This plot is determined using Eq. (4.9). The shunt resistance, R_{sh}, is open-circuited in all cases. 89

4.12 The power delivered to an external load as a function of the applied voltage for various selections of R_s. For the purposes of this analysis, I_o set to 10^{-9} A, I_L set to 100 mA, and the temperature set to 300 K. 91

4.13 The fill-factor, FF, as a function of the series resistance, R_s, for a photovoltaic solar cell, modeled as in Figure 4.9, as a function of the series resistance, R_s. For all cases, I_o is set to 10^{-9} A, I_L is set to 100 mA, and the temperature is set to 300 K. 92

4.14 The efficiency as a function of energy gap, E_g, for the AM0 and AM1.5 solar spectra. The efficiency corresponding to the blackbody solar spectra is also depicted. 94

4.15 This current-voltage device characteristic plotted as a function of the voltage across the p-n junction device terminals. For the purposes of this analysis, I_o is set to 10^{-9} A, I_{ro} is set to 1 μA, I_L is set to 100 mA, and the temperature is set to 300 K. 96

4.16 The power delivered to the external load as a function of the applied voltage across the terminals of the p-n junction. For all cases, I_o is set to 10^{-9} A, I_{ro} is set to 1 μA, I_L is set to 100 mA, and the temperature is set to 300 K. 98

4.17 Fill-factor as a function of I_L. Both the ideal case and the case with the recombination processes taken into account are considered. For all cases, I_o is set to 10^{-9} A, I_{ro} is set to 1 μA, I_L is set to 100 mA, and the temperature is set to 300 K. 99

List of Symbols

A ..... cross sectional area

$a(subscript)$ ..... acceptor, e.g., N_a is acceptor concentration

c ..... speed of light in vacuum

D_e ..... diffusion coefficient for electrons

D_h ..... diffusion coefficient for holes

$d(subscript)$ ..... donor, e.g., N_d is donor concentration

E ..... energy

$\vec{E}$ ..... electric field vector

E_{CN} ..... conduction band edge

E_{CP} ..... conduction band edge

E_F ..... Fermi energy level

E_g ..... bandgap energy

E_o ..... built-in electric field

$e(subscript)$ ..... electron

E_x ..... electric field in the x-direction

E_{VN} ..... valence band energy edge

E_{VP} ..... valence band energy edge

$E_f(f), E_\lambda(\lambda), E_\omega(\omega)$ ..... energy per electromagnetic mode

f ..... frequency

h ..... Planck's constant

$\hbar$ ..... reduced Planck constant

$\hbar\omega$ ..... photon energy

$h(subscript)$ ..... hole

I ..... electric current

I_L ..... photocurrent

I_o ..... scale current

I_{sc} ..... short-circuit current

$I(v)$ ..... current-voltage device characteristic

J_{Dx} ..... diffusion current density

J_{dx} ..... total current density

J_{eDx}, J_{hDx} . current density associated with electron diffusion, current density associated with holes diffusion

J_{edx}, J_{hdx} . current density associated with electron drift, current density associated with holes drift

J_o ..... scale current density

J_{recom} ..... recombination current density

J_{ro} ..... recombination scale current density

J_{so} ..... scale current density

$J(v)$ ..... total current density associated with current-voltage characteristics

J_x ..... total current density

k ..... the Boltzmann constant

L ..... length

L_e, L_h ..... electron diffusion length, hole diffusion length

n ..... electron concentration

N_d ..... donor and ionized donor concentrations

n_i ..... intrinsic concentration

n_M ..... concentration of electrons at the center of junction

n_{no}, p_{po} ..... equilibrium majority carrier concentrations

n_{po}, p_{no} ..... equilibrium minority carrier concentration

n_p ..... electron concentration

n_x ..... effect of confinement in x-direction

n_y ..... effect of confinement in y-direction

n_z ..... effect of confinement in z-direction

$\tilde{N}(\omega)$ ..... density of modes

$n_f(f), n_\lambda(\lambda), n_\omega(\omega)$ .....energy density per electromagnetic mode

P_{max} ..... maximum power

p ..... hole concentration

p_M ..... concentration of holes at the center of the junction

p_n ..... hole concentration

$p(v)$ ..... delivered power

$p_f(f), p_\lambda(\lambda), p_\omega(\omega)$ ... received power flux spectra in frequency, wavelength, angular frequency

q ..... electron charge

R_s ..... series resistance

R_{sh} ..... shunt resistance

r_s ..... radius of the Sun

r_{se} ..... radius of the Earth orbit

$S(\lambda)$ ..... solar spectrum

$\tilde{S}(\lambda)$ ..... integrated solar spectrum

T ..... temperature

t ..... time

t_i ..... time of the $i-th$ electron

u_{xi} ..... initial velocity in x-direction

V, v ..... voltage

V_o ..... built-in voltage

V_{oc} ..... open-circuit voltage

v_{edx}, v_{hdx} . electron drift velocity and hole drift velocity in the x-direction

v_{xi} ..... velocity in the x-direction

W_n, W_p ..... width of depletion region on the n-type side and on the p-type side with no applied voltage

Δ ..... excess charge carrier concentration

∇^2 ..... Laplacian operator $\nabla.\nabla$

ε ..... permittivity

ε_o ..... permittivity of free space

η ..... ideality factor

θ ..... angle

λ ..... wavelength

$\mu_f(f), \mu_\lambda(\lambda), \mu_\omega(\omega)$ ..... energy density associated with an electromagnetic cavity

μ_h, μ_e ..... hole drift mobility, electron drift mobility

ρ ..... resistivity

ρ_{net} ..... net space charge density

τ_e ..... electron lifetime

τ_h ..... hole lifetime

$\mathcal{E}_x$ ..... electric field in the x-direction

Φ_e ..... electron flux

Φ_h ..... hole flux

ω ..... angular frequency

Glossary

AM0 air mass zero

AM1 air mass one

AM1.5 air mass 1.5

ASTM American Society for Testing and Materials

c-Ge crystalline germanium

c-Si crystalline silicon

EJ Exajoules

FF fill-factor

NREL National Renewable Energy Laboratory

WWEA World Wind Energy Association

Acknowledgements

First and foremost, I want to thank my advisor, Dr. Stephen O'Leary. It has been an honor to be his MASc student. I gratefully appreciate his contributions, in terms of time, ideas, and funding. These made my MASc experience productive and stimulating. His advice and comments greatly helped me with my progress. I also appreciate his open mind and confidence, allowing me to propose and develop my own ideas. The joy and enthusiasm he has for his research was contagious and motivational for me, even during the tough times. I am also thankful for the excellent role model he has provided for me.

Lastly, I offer my regards and blessings to all those who supported me during the completion of this thesis.

Chapter 1

Introduction

The economic vibrancy of modern industrial economies requires access to cheap and abundant supplies of energy. Today, the uses of energy are numerous. Energy is needed for the transportation of goods and for manufacturing. It is also crucial for allowing habitation in regions of the Earth that are either too cold or too hot or both. The demand for energy continues to increase with each passing year; see Figure 1.1. In 2010, industrial societies consumed about 515 Exajoules (EJ) of energy; 1 Exajoule is equivalent to 10^{18} Joules (J). Projections suggest that the global demand for energy will exceed 700 EJ per year by the year 2030, a 36% increase over that consumed in 2010 [1]. Energy supplies fuel modern human civilization. Industrial societies would cease to function if sources of energy were no longer available.

There are a number of natural resources that may be drawn upon in order to generate energy. For the past century, fossil fuels have been the primary source of energy for modern industrial societies, such as Canada's [2]. Unfortunately, in recent years, the finiteness and non-renewable nature of this resource has become apparent [3]. Oil industry insiders suggest that "peak oil" will be achieved shortly. In addition, the demand for energy from emerging economies will rapidly deplete the reservoirs of fossil fuels that

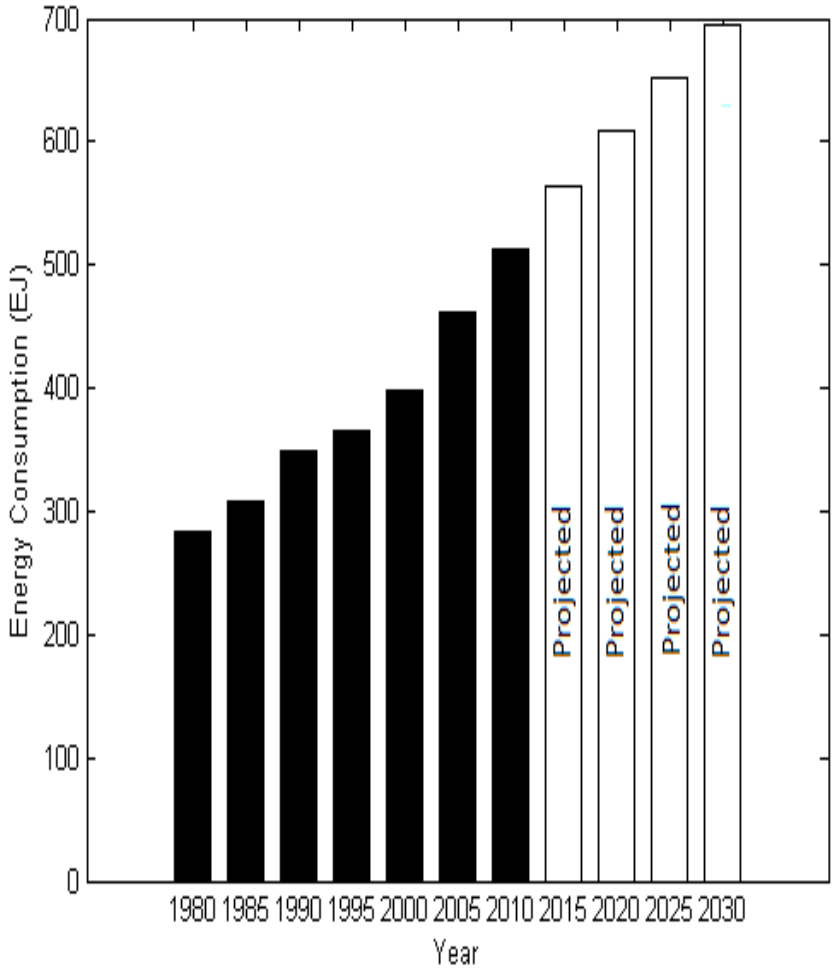

Figure 1.1: Worldwide energy consumption by industrial societies as a function of the year. The data depicted in this plot is from the US Department of Energy [1].

remain. The harmful emissions that arise as a corollary to the use of fossil fuels further underscores the urgent need to develop alternate and renewable sources of energy.

In actual fact, renewable sources of energy have been used since the dawn of human civilization. Throughout human history, flowing water has been used in order to supply energy needs. Flour mills of yore often used water in order to provide the mechanical energy needed for the flywheels and pulleys found within such plants [4]. More recently, flowing water has been used in order to supply electrical power. This type of electrical power is often referred to as hydroelectricity. The first use of hydroelectricity dates back as far as the 1870s [5]. Adam Beck's development of the Niagara Falls power station, the first large scale hydroelectrical generating station on Earth, further demonstrated the utility of hydroelectricity [6]. Similar projects have now been developed throughout the world. Unfortunately, this resource is now almost fully tapped, and new sources of renewable energy must also be considered [7].

While wind power has been used for many years, it is really only over the past two decades that wind power has been added to the energy mix as a viable candidate for the generation of renewable electrical power. This is particularly true in Europe, where tax incentives have created a large wind power industry. In Denmark, for example, wind power supplies as much as 20% of the electrical energy in the country [8]. In many jurisdictions within North America, windmills now dot the countryside [9], and wind power is now considered a serious potential source of renewable energy; at the present time, however, wind power only supplies 2 % of North Ameri-

can electrical power demands [10]. Unfortunately, there are some drawbacks associated with wind power that detract from its practicality. The wind is variable in its intensity, and thus, it can not be used in order to supply a steady source of power. The construction of wind turbines is costly and impacts upon the local environment. The noise that is produced as a result of wind power also has taken the sheen off this potential source of renewable energy [11].

The Sun produces a tremendous amount of energy. Arising as a product of thermonuclear fusion processes within it, the solar radiation that is emitted from the Sun is mostly in the form of electromagnetic waves [12]. The Earth receives a solar flux of roughly 1400 W/m^2 [13]. This radiation furnishes the Earth with the energy that the life forms on the Earth require. It is responsible for supplying the Earth with warmth and for photosynthesis, which is the process that allows plants to grow; photosynthesis converts solar radiation into organic compounds, which is ultimately the energy source that plants draw upon for sustenance. Estimates suggest that the Earth receives about 5.6 million EJ of solar radiation per year [14]. If completely harnessed, this would supply in excess of 10000 times of all of humanity's energy needs today.

Solar radiation may be harnessed through the use of solar cells. A photovoltaic solar cell is comprised of semiconducting materials prepared in the form of a p-n junction. Photovoltaic solar cells aim to generate electrical power in response to exposure to the Sun's rays. Solar radiation corresponds to a flux of photons, and when these photons are sufficiently energetic, electron-hole pairs can be generated within the semiconductor.

Through the application of a potential across such a solar cell, electrical power can be drawn from the solar cell. The first modern photovoltaic solar cell was that fabricated in 1954 by Pearson, Chapin, and Fuller of Bell Telephone Laboratories [15]. This prototype crystalline silicon (c-Si) based solar cell, which was based on the p-n junction architecture, was reported to have an initial efficiency of 4.5 %. Subsequent improvements, that were introduced in the following months, allowed this efficiency to increase to 6 % [16]. Improvements in the materials used and the device geometries employed, that have been introduced over the past half century, have led to dramatic improvements in the resultant c-Si based solar cell efficiencies, as may be seen from Figure 1.2 [17].

Fundamentally, a modern photovoltaic solar cell is a semiconductor p-n junction. That is, it is comprised of a p-type semiconductor region that is directly abutted against an n-type semiconductor region. Such junctions are found frequently in the microelectronics industry, and the fact that the fabrication processes that are employed in their manufacturing are well-developed further adds to the practicality of this particular solar cell device configuration. When exposed to sunlight, the absorption of the photons within the sunlight by the semiconductor leads to the generation of electron-hole pairs within the semiconductor. These charge carriers are then separated under the action of the electric field. The potential difference that develops between these separated charge carriers, coupled with the resultant photocurrent, are what is responsible for the generation of electrical power from such a solar cell.

A p-n junction is comprised of both neutral and space-charge regions, as

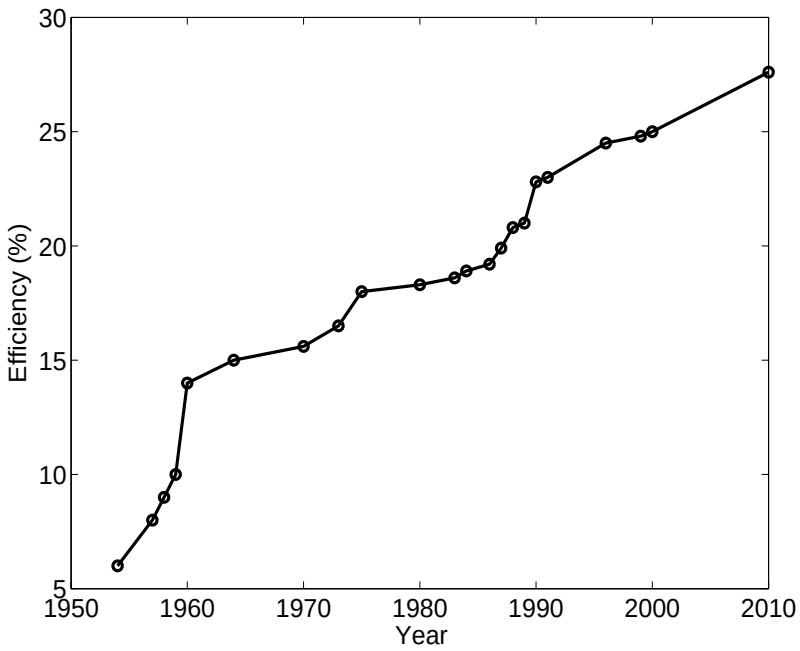

Figure 1.2: The efficiency of c-Si based solar cells as a function of the year. The data is taken from Hezel [17].

is shown in Figure 1.3. The space-charge region is formed in the immediate locality of the interface between the p-type and n-type semiconductor regions. The neutral regions lie on either side of this space-charge region. The minority charge carriers within both the p-type and n-type semiconductor regions are ultimately what are responsible for the external photocurrent. To zeroth-order, the minority charge carriers within the neutral regions, that are primarily engaging in diffusion processes, may be considered as being supplied by the external current. If the recombination that occurs within the space-charge region is taken into account, however, the external current must also supply the charges that are lost due to recombination within the space-charge region. As photovoltaic solar cells are fabricated using a p-n junction configuration, it is clear that recombination processes are likely to play an important role in determining the performance of such a cell.

This thesis is organized in the following manner. In Chapter 2, a brief review of the developments in solar cell technology, that have transpired over the years, is provided. In addition, a detailed description of the solar spectrum is furnished within this chapter, this providing a measure of how the power provided by the Sun is distributed over the electromagnetic spectrum. Then, in Chapter 3, the operating principles of the p-n junction are discussed, the photovoltaic solar cell being based on the p-n junction architecture. In Chapter 4, the p-n junction operating principles are employed in concert with the solar spectrum in order to analyze the performance of a photovoltaic solar cell. The impact of recombination processes on these results is also examined. Finally, in Chapter 5, conclusions are drawn and recommendations for further research are suggested.

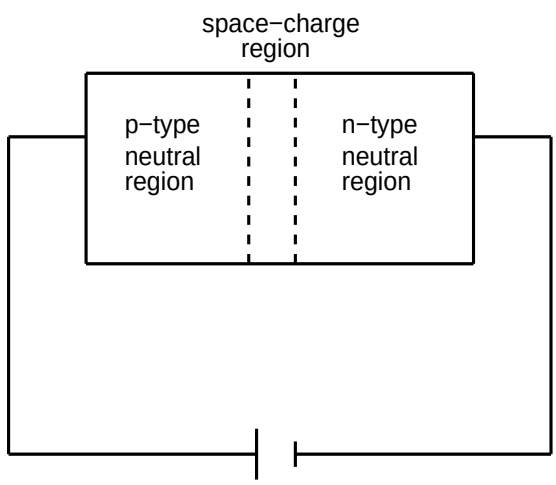

Figure 1.3: A schematic of a p-n junction. The p-type region is abutted next to the n-type region. The neutral and space-charge regions are depicted.

Chapter 2

The solar spectrum and background material

2.1 Background

Modern photovoltaic solar cells are based upon the p-n junction configuration. Semiconductors, such as silicon or germanium, are the materials from which these junctions are fabricated. When the Sun's radiation impinges upon such a junction, photons, with energies that exceed the energy gap of the underlying semiconductor, generate electron-hole pairs. The "built-in" electric field, associated with the space-charge region at the p-n junction interface, separates these charge carriers. As a consequence, a potential difference arises across the two electrodes of the junction. This phenomenon is referred to as the "photovoltaic effect," and, as a result of it, exposure of such a junction to light leads to the generation of current [15]. The resultant current is referred to as a photocurrent, as it is ultimately related to light exposure. The power delivered from the photovoltaic solar cell is essentially proportional to the product of the photocurrent and the potential difference across the junction.

In order for a photovoltaic solar cell to work properly, it should per-

form four essential functions: (1) light absorption, (2) charge carrier generation, (3) charge carrier separation, and (4) and charge carrier collection [15]. These functions allow a photovoltaic solar cell to supply electrical power to a load. Light absorption arises as a consequence of the interaction of a beam of light with condensed matter, i.e., the semiconductor. As the light beam passes through the material, its intensity diminishes in an exponential fashion. The attenuation of light is directly related to the generation of electron-hole pairs within the material. Photons in the light beam with energies that exceed the energy gap of the semiconductor can lead to the creation of electron-hole pairs. These pairs of charge carriers, which typically recombine when equilibrium is achieved, separate under the action of the "built-in" electric field that exists across the p-n junction; with light exposure generating excess charge carriers, the "built-in" junction is not in equilibrium. In order for these charge carriers to contribute to the external photocurrent, these charge carriers must drift under the action of the electric field within the bulk of the p-n junction, i.e., away from the p-n junction interface towards the external contacts.

This chapter is organized in the following manner. In Section 2.2, a brief overview of solar cell technological developments, that have transpired since their introduction, is provided. Then, in Section 2.3, an examination of the energy in the Sun's electromagnetic rays is furnished. A number of solar spectra are then defined in Section 2.4. Finally the integrated solar spectrum is introduced in Section 2.5.

2.2 Solar cell technology developments

In 1839, the French physicist, A. E. Becquerel, demonstrated the photovoltaic effect. In particular, while studying the properties of electrolytic cells, Becquerel noted that an electrical current is produced when such cells are exposed to light [5]. In contrast, with no light exposure, the electrical current was found to be nil. As this current is directly related to the presence of light, it was dubbed a photocurrent. In 1876, A. William and R. Day observed a photocurrent within the semiconductor selenium [5]. Later on, in 1894, C. Fritts developed what would later be referred to as a photovoltaic solar cell, comprised of a junction of selenium coated with gold. The efficiency of this cell was about 1 % [15]. While not as efficient as modern photovoltaic solar cells, Fritts's development was an impressive 19th Century engineering innovation.

In the 1950s, c-Si based p-n junctions were being mass produced for a wide variety of electron device applications. As a result, it was just a matter of time before the photovoltaic solar cell was implemented in a c-Si based p-n junction technology. The first successfully implemented c-Si based photovoltaic solar cell was that fabricated in 1954 at Bell Telephone Laboratories by Pearson, Chapin, and Fuller [15]. This cell, which was based upon the p-n junction architecture, had an initial efficiency which was reported to be about 4.5 %. Later on, however, with improvements in the device design, a 6 % efficiency was achieved. Initial applications for photovoltaic solar cells focused on the emerging space-program and military applications. The first commercial applications for this emerging solar cell technology were found

in commercial satellites, that were starting to be deployed during the late 1960s. Satellites needed sustainable means of supplying their energy needs, and solar cells filled this niche very effectively. The first commercial satellite to be powered using solar cells was Telstar from the American Telegraph and Telecommunications Company, the parent company of Bell Telephone Laboratories. This satellite was placed in Earth orbit in 1962 [8].

Owing to their great cost, solar cells were initially not employed in consumer electronic products. This has changed over time, however, as solar cell technology, and the materials related to solar cells, have become more widely available. Initial applications of solar cell technology in consumer electronic goods occurred in the mid-1970s (they were initially deployed in watches and calculators) and now solar cells are a staple of the consumer electronic products that are available. Recently, solar cells based on different semiconductor materials, such as cadmium sulphide, gallium arsenide, and cadmium telluride, have been employed in order to achieve higher efficiencies than that achieved previously through c-Si based solar cells [15]. Gains, in terms of cost-reductions and economies of scale, have also been achieved. In addition to the burgeoning scope of consumer electronic products that employ solar cell technology, since the 1990s photovoltaic solar cells have been fabricated for telecommunication and localized power supply applications [15]. Recently, there has been interest in using photovoltaic solar cells for supplying electricity to the grid [15]. In 2000, the first photovoltaic solar cell production plant, that aimed to produce photovoltaic solar cells for mass power generation purposes, was built in Perrysburg, Ohio [8]. Most recently, research, in terms of photovoltaic solar cells, has focused upon fabricating

solar cells of improved geometries and with different materials in order to achieve higher efficiencies and greater cost effectiveness [15].

2.3 Blackbody radiation

The power within the Sun's rays may be characterized by the solar spectrum, which provides for the distribution of power over the electromagnetic spectrum. Often times, insights into the spectral dependence of this power spectrum may be achieved by treating the Sun as a blackbody, a blackbody absorbing all of the radiation that it receives. While the Sun is not exactly a blackbody, the blackbody approximation works quite well and provides insight into the spectral dependence of the solar spectrum. It is therefore instructive to consider the power spectrum corresponding to a blackbody.

For steady-state sinusoidal excitations, of angular frequency, ω, in a vacuum, the equation for the electric field, $\vec{\mathbf{E}}$, may be expressed as

$$\nabla^2 \vec{\mathbf{E}} = -\frac{\omega^2}{c^2}\vec{\mathbf{E}}, \tag{2.1}$$

where c represents the speed of light in vacuum. For an electromagnetic cavity, of dimensions $L \times L \times L$, as shown in Figure 2.1, for zero-field along the boundaries, the possible solutions for Eq. (2.1), for all dimensions, i.e., E_x, E_y, and E_z, where $\vec{\mathbf{E}} = (E_x, E_y, E_z)$, are of the form [18],

$$E(x, y, z) = A \sin\left(\frac{n_x \pi x}{L}\right) \sin\left(\frac{n_y \pi y}{L}\right) \sin\left(\frac{n_z \pi z}{L}\right), \tag{2.2}$$

where A is a constant and n_x, n_y, and n_z are integers which are greater than or equal to unity. Substituting Eq. (2.2) into Eq. (2.1), it may be seen that

$$\frac{\omega^2}{c^2} = \left(\frac{n_x \pi}{L}\right)^2 + \left(\frac{n_y \pi}{L}\right)^2 + \left(\frac{n_z \pi}{L}\right)^2. \tag{2.3}$$

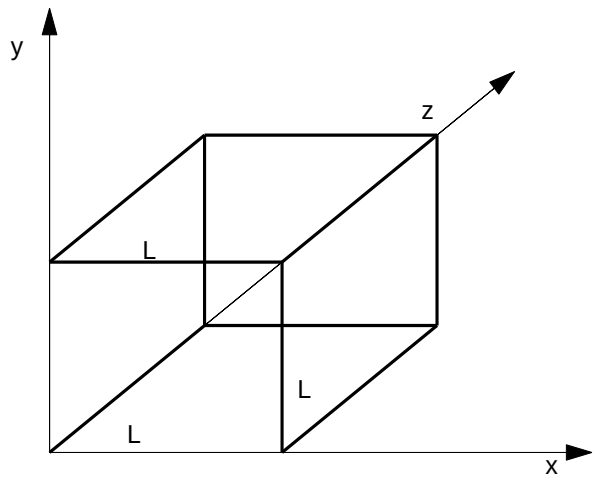

Figure 2.1: A three dimensional electromagnetic cavity of the dimensions $L \times L \times L$.

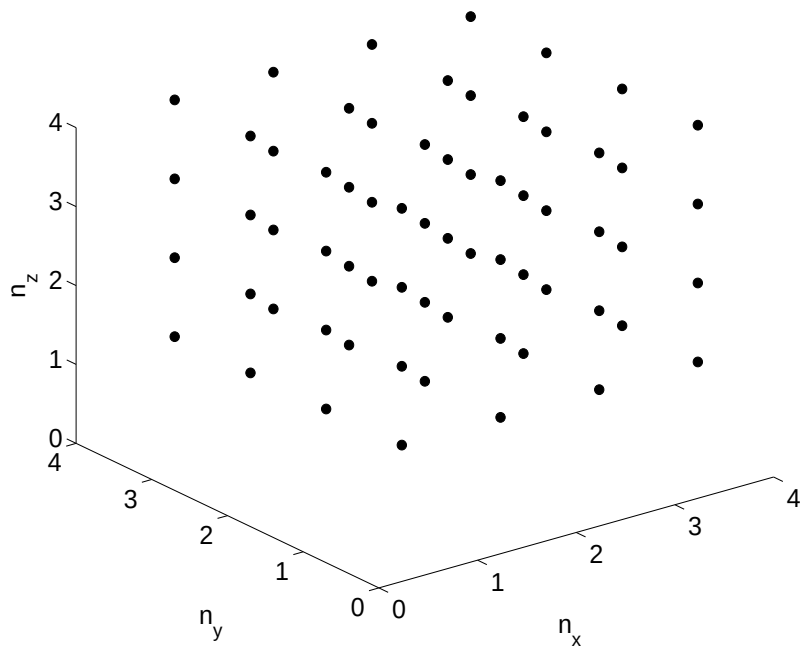

Figure 2.2: Points in n-space. Each point corresponds to an allowed set of n_x, n_y, and n_z values, corresponding to a possible solution of Eq. (2.1).

In n-space, which is depicted in Figure **??**, there is a unit density of points in the first octet, i.e, there is one point for every combination of n_x, n_y, and n_z, where these quantities are integers. In the continuum limit, i.e, when n_x, n_y, and n_z become large, the number of points with angular frequency less than a given value of ω,

$$\tilde{N}(\omega) = \frac{1}{8}\frac{4\pi}{3}n^3, \tag{2.4}$$

where

$$n^2 = n_x^2 + n_y^2 + n_z^2. \tag{2.5}$$

Noting, from Eq. (2.3), that

$$\frac{\omega^2}{c^2} = \frac{\pi^2}{L^2}n^2, \tag{2.6}$$

it is seen that

$$\tilde{N}(\omega) = \frac{1}{8}\frac{4\pi}{3}\left(\frac{\omega^2 L^2}{c^2\pi^2}\right)^{3/2}. \tag{2.7}$$

This suggest that a density of modes may be defined, i.e, where $n_\omega(\omega)\Delta\omega$ corresponds to the number of electromagnetic modes in the cavity, between $[\omega, \omega+\Delta\omega]$, per unit volume [18]. Given that every n_x, n_y, and n_z selection corresponds to two possible electromagnetic modes, i.e, two different polarizations, differentiation of Eq. (2.7), multiplication by a factor of 2, and division by the volume, L^3, results in

$$n_\omega(\omega) = \frac{\omega^2}{c^3\pi^2}. \tag{2.8}$$

It is often the case that one must instead determine the distribution of

modes over frequency or wavelength. Noting that

$$f = \frac{\omega}{2\pi}, \tag{2.9}$$

and that

$$f\lambda = c, \tag{2.10}$$

two alternate density of modes distribution functions may also be introduced, $n_f(f)$ and $n_\lambda(\lambda)$, where $n_f(f)\Delta f$ and $n_\lambda(\lambda)\Delta\lambda$ denote the number of electromagnetic modes, per unit volume, between $[f,\ f+\Delta\ f]$ and $[\lambda,\ \lambda+\Delta\lambda]$, respectively. Thus,

$$n_f(f) = \frac{8\pi f^2}{c^3}, \tag{2.11}$$

while

$$n_\lambda(\lambda) = \frac{8\pi}{\lambda^4}. \tag{2.12}$$

These functions, $n_\omega(\omega)$, $n_f(f)$, and $n_\lambda(\lambda)$, provide for the density of electromagnetic modes, per unit volume, with respect to ω, f, and λ, respectively.

The density of electromagnetic modes, $n_\omega(\omega)$, may now be employed in the determination of the energy density. In particular, it may be shown that the energy density

$$u_\omega(\omega) = n_\omega(\omega)E(\omega), \tag{2.13}$$

where $u_\omega(\omega)\Delta\omega$ represents the energy, per unit volume, between angular frequencies $[\omega,\ \omega+\Delta\omega]$, and $E(\omega)$ denotes the energy per electromagnetic mode of angular frequency ω. Classically, it may be shown that the energy per electromagnetic mode is kT, where T represents the temperature and k denotes the Boltzmann constant, i.e.,

$$u_\omega(\omega) = \frac{1}{\pi^2}\frac{w^2}{c^3}kT. \tag{2.14}$$

In a similar sense, the energy density, with respect to frequency and wavelength, $u_f(f)$ and $u_\lambda(\lambda)$, respectively, may be expressed as

$$u_f(f) = \frac{8\pi f^2}{c^3} kT, \tag{2.15}$$

and

$$u_\lambda(\lambda) = \frac{8\pi}{\lambda^4} kT, \tag{2.16}$$

where $u_f(f)\Delta f$ and $u_\lambda(\lambda)\Delta\lambda$ represent the energy, per unit volume, between $[f,\ f{+}\Delta f]$ and $[\omega,\ \omega{+}\Delta\omega]$, respectively. Unfortunately, the classical energy distributions, $u_\omega(\omega)$, $u_f(f)$, and $u_\lambda(\lambda)$, depicted in Eqs. (2.14), (2.15), and (2.16), respectively, exhibit a non-integrable singularity at high frequencies or low wavelengths. This was referred to as the ultraviolet catastrophe in the 19th Century scientific community [19]. Of course, the integration of the energy spectrum of a blackbody object is in actuality finite, this being experimentally known in the 19th Century. The reasons why the ultraviolet catastrophe does not occur were accounted for in the early 20th Century, and the phenomena underlying these reasons led to a revolution in physics that continues today.

In 1900, Planck suggested that light was actually comprised of photons, and that each photon has a discrete energy, which is linearly proportional to its angular frequency, ω [19]. Introducing a constant, now referred to as Planck's constant, h, the corresponding photon energy may be expressed as $\hbar\omega$, where $\hbar$ is referred to as the reduced Planck's constant, i.e.,

$$\hbar \equiv \frac{h}{2\pi}. \tag{2.17}$$

Through a statistical analysis, Planck was able to demonstrate that

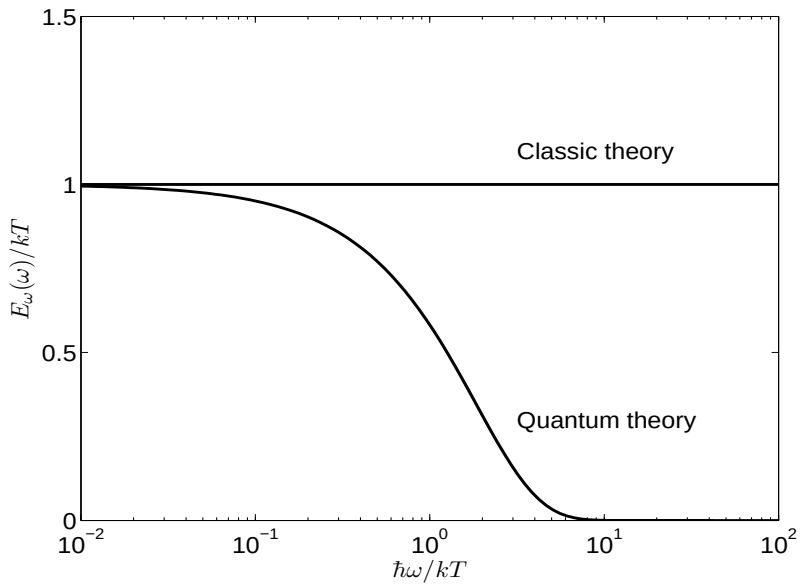

Figure 2.3: The energy per electromagnetic mode as a function of $\frac{\hbar\omega}{kT}$. The classical result is contrasted with that due to Planck. The results are presented in a dimensionless form through a divison by the classical result, kT.

$$E_\omega(\omega) = \frac{\hbar\omega}{\exp\left(\frac{\hbar\omega}{kT}\right) - 1}. \tag{2.18}$$

In Figure 2.3, the energy per mode is plotted as a function of the photon energy, $\hbar\omega$. The classical result, kT, is also depicted, it being independent of $\hbar\omega$; this spectral dependence is normalized with the respect to the classical result, kT, i.e., the results are presented in a dimensionless form. It is noted that as $\hbar\omega$ becomes very large, the energy per electromagnetic mode diminishes, eventually becoming negligible. This allows for a reconciliation between theory and experiment, i.e., the ultraviolet catastrophe is eliminated through the exponential decrease in $E_\omega(\omega)$ as $\omega \to \infty$, i.e., the resultant function, $u_\omega(\omega)$, is now integrable. It is noted that in the classical limit, i.e., when $\hbar \to 0$, Eq. (2.18) reduces to the classical result, i.e.,

$$E_\omega(\omega) \to kT. \tag{2.19}$$

This is consistent with the general observation that all quantum results reduce to their corresponding classical results as $\hbar \to 0$, i.e., as one moves towards the classical limit.

In the f representation

$$E_f(f) = \frac{hf}{\exp\left(\frac{hf}{kT}\right) - 1}, \tag{2.20}$$

while in the λ representation

$$E_\lambda(\lambda) = \frac{hc}{\lambda\left[\exp\left(\frac{hc}{k\lambda T}\right) - 1\right]}, \tag{2.21}$$

where $E_f(f)$ and $E_\lambda(\lambda)$ represent the energy per electromagnetic mode. Using the Planck result for $E_\omega(\omega)$, i.e., Eq. (2.18), from Eqs. (2.8) and (2.13),

the energy density associated with an electromagnetic cavity may be expressed as

$$u_\omega(\omega) = \frac{1}{\pi^2 c^3}\left(\frac{\hbar\omega^3}{\exp\left(\frac{\hbar\omega}{kT}\right)-1}\right). \tag{2.22}$$

A similar analysis, performed in the f representation, yields

$$u_f(f) = \frac{8\pi f^2}{c^3}\left(\frac{hf}{\exp\left(\frac{hf}{kT}\right)-1}\right), \tag{2.23}$$

where Eq. (2.23) is determined from the product of Eqs. (2.11) and (2.20). In the wavelength representation, however,

$$u_\lambda(\lambda) = \frac{1}{\lambda^5}\left(\frac{8\pi hc}{\exp\left(\frac{hc}{\lambda kT}\right)-1}\right), \tag{2.24}$$

where Eq. (2.24) is determined from the product of Eqs. (2.12) and (2.21). It is noted that all of the energy distribution functions, i.e., $u_\omega(\omega)$, $u_f(f)$, and $u_\lambda(\lambda)$, are now integrable. The distribution of energy of an electromagnetic cavity, is plotted as a function of wavelength in Figure 2.4, for both the classical and quantum cases, i.e., Eqs. (2.16) and (2.24), respectively. The temperature is set to the surface temperature of the Sun, i.e., 5780 K, for the purposes of this analysis. The ultraviolet catastrophe is seen at low wavelengths for the classical result [20].

It can be shown that the power flux produced by a blackbody object is related to the energy density within the cavity. In particular, we have

$$p_\omega(\omega) = u_\omega(\omega)\frac{c}{4}, \tag{2.25}$$

where $p_\omega(\omega)\Delta\omega$ represents the power emitted, between $[\omega, \omega+\Delta\omega]$, per unit area; the power flux refers to the projected power, per unit area, that is

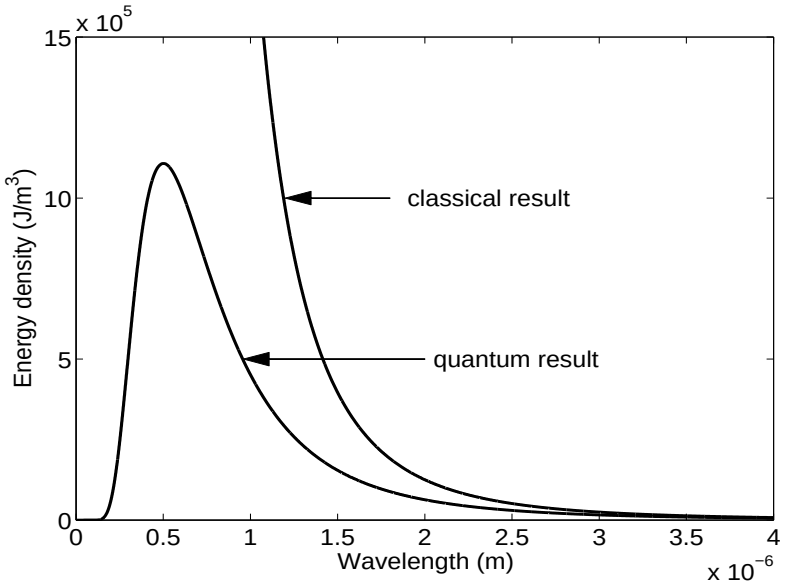

Figure 2.4: The energy density in an electromagnetic cavity as a function of the wavelength. The temperature is set to 5780 K for the purposes of this analysis. The classical result, i.e., Eq (2.16), is contrasted with result of Planck, i.e., the quantum result, Eq (2.24).

radially emitted. Using Eqs. (2.22) and (2.25), it can be shown that

$$p_\omega(\omega) = \frac{1}{4\pi^2 c^2}\left(\frac{\hbar\omega^3}{\exp\left(\frac{\hbar\omega}{kT}\right) - 1}\right), \tag{2.26}$$

where integration over this power spectrum leads to the total power radiated from the blackbody object, per unit area. A similar analysis may be used to show that in the f representation,

$$p_f(f) = \frac{2\pi f^2}{c^2}\left(\frac{hf}{\exp\left(\frac{hf}{kT}\right) - 1}\right), \tag{2.27}$$

where $p_f(f)\Delta f$ provides for the power emitted, between frequencies $[f, f + \Delta f]$, per unit area. In the λ representation, however,

$$p_\lambda(\lambda) = \frac{1}{\lambda^5}\left(\frac{2\pi hc^2}{\exp\left(\frac{hc}{\lambda kT}\right) - 1}\right), \tag{2.28}$$

where $p_\lambda(\lambda)\Delta\lambda$ provides for the power emitted, between wavelengths $[\lambda, \lambda + \Delta\lambda]$, per unit area. All of these power flux spectra are seen to be integrable.

The expressions for the power flux spectra that have been determined correspond to the surface of the blackbody. The solar flux received by the Earth is attenuated, of course. Assuming that the solar radiation emitted from the Sun is projected radially from the surface of the Sun, if the Earth orbits the Sun at a radius r_{se}, and if the Sun itself has a radius r_s, then the power flux received at the periphery of the Earth's atmosphere is reduced by an attenuation factor of $\left(\frac{r_s}{r_{se}}\right)^2$, as seen in Figure 2.5 [21]. That is, in the ω representation, the power flux spectra, received by the periphery of the Earth's atmosphere, may be expressed as

$$p_\omega(\omega) = \frac{1}{4\pi^2 c^2}\left(\frac{r_s}{r_{se}}\right)^2\left(\frac{\hbar\omega^3}{\exp\left(\frac{\hbar\omega}{kT}\right) - 1}\right). \tag{2.29}$$

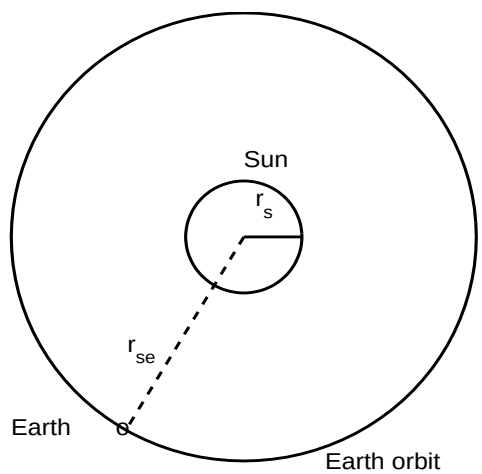

Figure 2.5: The Earth orbiting the Sun at radius r_{se}. The radius of the Sun itself is r_s. These distances have been exaggerated on this figure for the purposes of illustration.

In the f representation, however, this received power flux spectra may instead be expressed as

$$p_f(f) = \frac{2\pi f^2}{c^2}\left(\frac{r_s}{r_{se}}\right)^2\left(\frac{hf}{\exp\left(\frac{hf}{kT}\right)-1}\right). \tag{2.30}$$

In the λ representation, this received power flux spectra may be expressed as

$$p_\lambda(\lambda) = \left(\frac{r_s}{r_{se}}\right)^2 \frac{2\pi hc^2}{\lambda^5\left[\exp\left(\frac{hc}{\lambda kT}\right)-1\right]}. \tag{2.31}$$

The temperature in these expressions, i.e., Eqs. (2.29), (2.30), and (2.31), corresponds to that at the surface of the blackbody, i.e., the surface of the Sun, as thermal equilibrium is achieved with the surrounding environment through this surface. It is seen that these power spectra are strong functions of this temperature. Treating the Sun as a blackbody, the power spectrum of the solar flux received by the periphery of the Earth's atmosphere, i.e., the solar spectrum, is a strong function of the temperature of the surface of the Sun. In the λ representation, i.e., Eq. (2.31), the variations exhibited by this power spectrum to changes in the Sun's surface temperature are depicted in Figure 2.6. For the purposes of this analysis, the radius of the Sun, r_s, is set to be 700×10^3 km, while the radius of the Earth orbit, r_{se}, is taken to be 150×10^6 km.

2.4 The solar spectrum

The solar spectrum characterizes the distribution of power within the electromagnetic radiation received from the Sun by the Earth. This electromagnetic radiation is comprised of both electric and magnetic field compo-

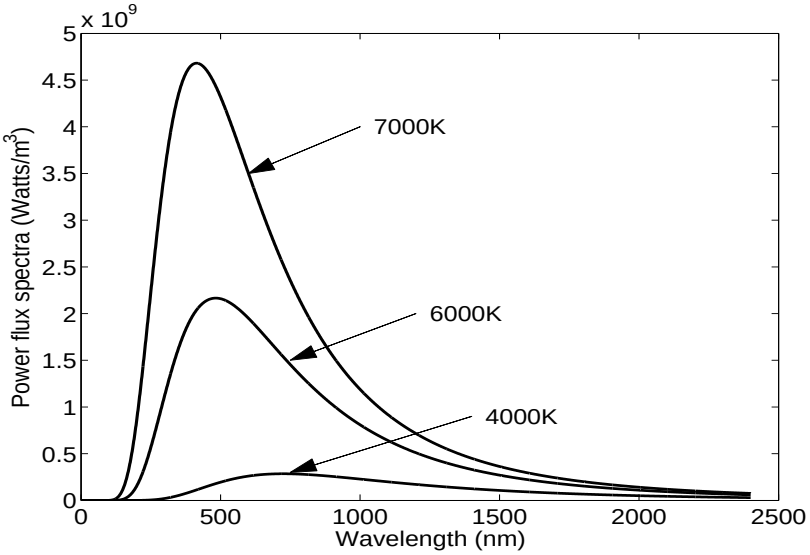

Figure 2.6: The solar spectrum, i.e., the power flux spectrum received at the periphery of the Earth's atmosphere, as a function of wavelength of blackbody radiation for different temperatures. These temperatures correspond to the temperature of the surface of the Sun. Eq. (2.31) is used for the purposes of this analysis, where r_s is set to 7.0×10^5 km and r_{se} is set to 1.5×10^8 km.

nents, and it reaches the Earth after propagating from the Sun to the Earth through space. It is instructive to define the spectral intensity of the solar radiation received by the Earth in terms of the "air mass" that the Sun's rays encounter. The air mass takes into account the losses that occur as a consequence of the propagation of the Sun's electromagnetic flux through the Earth's atmosphere. Losses arise as a result of the interactions of the electromagnetic radiation from the Sun with aerosol particles, gas molecules, and cloud droplets [22].

At the periphery of the Earth's atmosphere, the solar spectrum is as determined by the Sun, and the distance of the Earth's orbit from the Sun. It should be noted, however, that slight deviations from the blackbody spectrum, arising from absorption processes within the Sun's atmosphere itself, do occur. As a result, at the periphery of the Earth's atmosphere, the solar spectrum appears slightly different from that of a blackbody with an appropriately selected Sun surface temperature [23]. The intensity of the solar radiation received at the periphery of the Earth's atmosphere is referred to as air mass-zero (AM0), i.e., the sunlight has passed through zero of the Earth's atmospheric mass. In contrast, at the Earth's surface, when the Sun is directly overhead, the Sun's rays have traveled through one atmosphere. The resultant solar spectrum is referred to as air mass-one (AM1), and it will have a lower intensity than the AM0 solar spectrum, i.e., propagating through the Earth's atmosphere will lead to an attenuation in the received solar spectrum, this attenuation being non-uniformly distributed over the electromagnetic spectrum [22].

If the Sun's radiation is received at an oblique angle, then the Sun's

rays will effectively have passed through more than one atmosphere. Air mass-1.5 (AM1.5), a commonly used reference solar spectrum, refers to the solar radiation received by the surface of the Earth when the angle of incidence for the solar radiation is such that the Sun's rays effectively have passed through 1.5 atmospheres. This corresponds to roughly a 48.2° angle of incidence with respect to the vertical axis; see Figure 2.7. In general, the air mass can be defined in terms of the angle between the Sun's rays and the vertical axis, i.e., the axis normal to the surface of the Earth. That is,

$$\text{AM(number)} = \frac{1}{cos(\theta)}, \tag{2.32}$$

where θ refers to the angle of incidence with respect to the vertical axis, i.e., $\theta = 0^0$ corresponds to the Sun's rays coming in from directly overhead. The AM0 and AM1.5 solar spectra are depicted in Figure 2.8. The corresponding blackbody radiation spectrum is also depicted in Figure 2.8, where the surface temperature of the Sun is set to be 5780 K [23], this being a typical value found in the literature. Integration over these solar spectra, over the entire range of wavelengths, leads to the power flux densities tabulated in Table 2.1. Further details are discussed in the literature.

2.5 Integrated solar spectrum

In the analysis of a photovoltaic solar cell, it is instructive to determine the integrated solar spectrum. In the λ representation, the integrated solar spectrum.

$$\tilde{S}(\lambda) \equiv \int_0^{\lambda} S(\lambda) d\lambda, \tag{2.33}$$

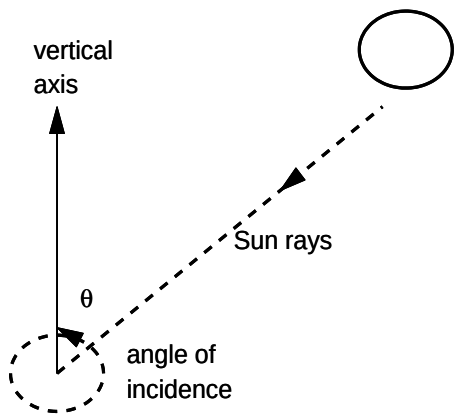

Figure 2.7: The angle of incidence, the vertical axis, and the direction of the Sun's rays.

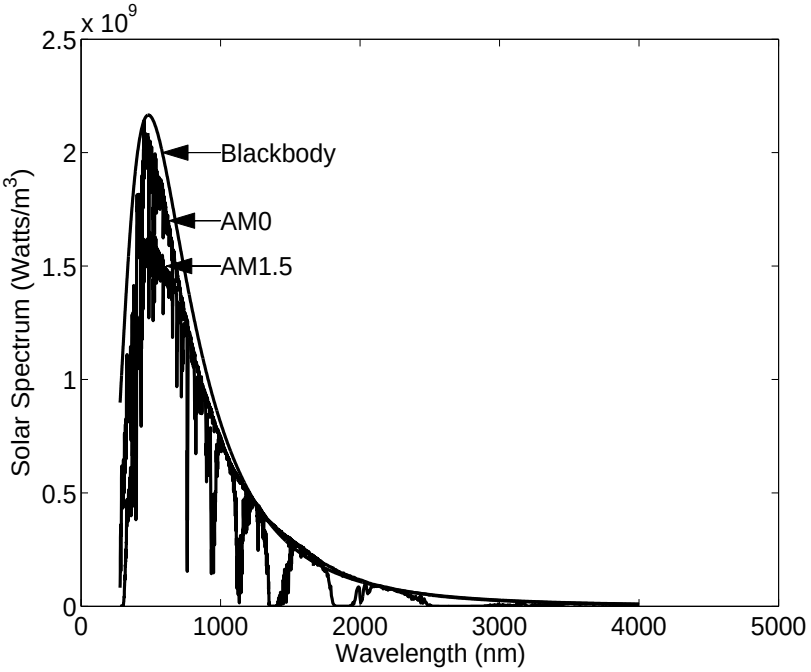

Figure 2.8: The solar spectra corresponding to the AM0 and AM1.5 cases. The experimental data is taken from NREL [24]. The blackbody solar spectrum is also depicted, for the Sun's surface temperature set to 5780 K [23].

Table 2.1: The integrated solar spectra obtained for the upper wavelength in Eq. (2.33) being set to ∞. This corresponds to integrating the solar spectra over the entire range of wavelengths.

Solar Condition	Power flux density (W/m^2)
AM0	1366.1
AM1.5	1000.13
Blackbody	1534.4

where $S(\lambda)$ denotes the solar spectrum itself. The integrated solar spectra, corresponding to the AM0 and AM1.5 solar spectra depicted in Figure 2.8, are shown in Figure 2.9. The integrated blackbody solar spectrum is also depicted in Figure 2.9 for the case of the surface temperature of the Sun being set to 5780 K [23]. It is noted that as the upper wavelength in the integration of the solar spectrum, i.e., as seen in Eq. (2.33), approaches infinity, the power densities, tabulated in Table 2.1, are achieved. A similar analysis may be performed in the ω and f representations, of course.

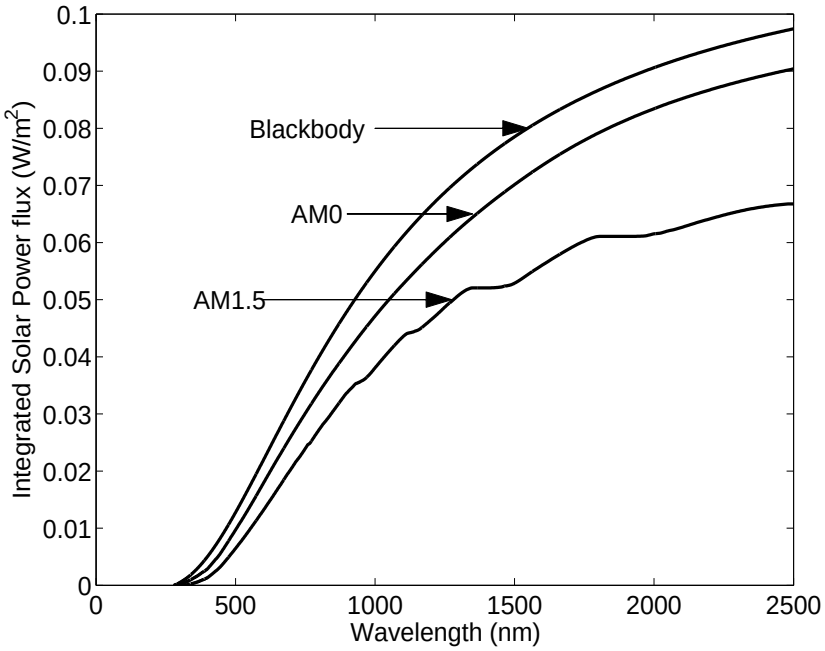

Figure 2.9: The integrated solar spectra corresponding to the AM0 and AM1.5 solar spectra. The integrated blackbody solar spectrum is also depicted for the Sun's surface temperature set to 5780 K [23].

Chapter 3

General theory of the p-n junction with recombination

3.1 Rationale

The fundamental building block of most semiconductor devices is the p-n junction. This junction forms the cornerstone upon which modern microelectronics is built. Accordingly, an understanding of the physics underlying p-n junctions is an important step to developing an appreciation for the operation of modern electron devices. Given that the p-n junction lies at the heart of the modern photovoltaic solar cell, understanding the behavior of the p-n junction is also crucial to the understanding of the operation of such a cell. In 1951, Shockley introduced a theory for the operation of the p-n junction, and described the current-voltage device characteristics of the resultant electron device [25]. This theory remains at the core of our understanding of the operation of such devices today.

In this chapter, the general operating principles of the p-n junction are laid out. Rather than going through all of the details provided for in the analysis of Shockley [25], instead only details relevant to photovoltaic solar cell modeling are provided. In particular, the analysis starts with a dis-

cussion on the geometric layout of the p-n junction. Then, the drift and diffusion charge carrier transport processes, that occur within a p-n junction, are presented. The behavior of the p-n junction under no bias is then discussed. The forward biased p-n junction behavior is then reviewed, an expression for the current-voltage device characteristic being obtained. The behavior of the p-n junction under reverse bias is also presented. Finally, the role that recombination processes play in influencing these device characteristics is discussed.

This chapter is organized in the following manner. In Section 3.2, the geometric layout of the p-n junction is reviewed. The drift and diffusion charge carrier transport processes, that occur within a p-n junction, are then discussed in Section 3.3. The behavior of the p-n junction under no bias is then presented in Section 3.4. The forward biased p-n junction is reviewed in Section 3.5, a current-voltage device characteristic being determined for the case of no recombination. The reverse biased p-n junction is then considered in Section 3.6. Finally, the role that recombination processes play in influencing these device characteristics is considered in Section 3.7.

3.2 The geometric layout of the p-n junction

In general, the p-n junction consists of a p-type semiconductor that is directly abutted against an n-type semiconductor. Most often, a common crystal is used, although heterogeneous p-n junctions have been fabricated. The p-type region is created by doping the underlying semiconductor material with acceptors, while the n-type region is created by doping the under-

lying semiconductor material with donors; for the case of c-Si, boron and phosphorous are commonly used acceptors and donors, respectively [26]. The transition between the p-type and n-type regions can be abrupt, or it can be of a gentler grade; the metallurgical junction represents the boundary junction between the p-type and n-type regions. While most p-n junctions are one-dimensional in nature, two-dimensional and three-dimensional p-n junctions have also been used in order to produce photovoltaic solar cells. The geometric layout of a one-dimensional abrupt p-n junction is depicted in Figure 3.1.

3.3 Drift and diffusion processes

There are two kinds of charge carriers within semiconductors, electrons and holes. These charge carriers engage in charge transport process that determine the performance of the resultant electron device. There are two fundamental charge carrier transport processes that influence the behavior of a p-n junction: 1) drift, in which the charge carriers transit and under the action of the applied electric field, and 2) diffusion, in which natural equilibrium processes act to redistribute the charge carriers within the semiconductor. In this section, these processes are discussed. How these processes influence the behavior of the resultant p-n junction will be considered later.

Consider an ensemble of N electrons. Electrons in an ensemble are in a perpetual state of motion and they frequently engage in scattering. Between scattering events, they act as free particles. It will be assumed that the $i-th$ electron begins its transit at $t = t_i$, where t_i denotes the time

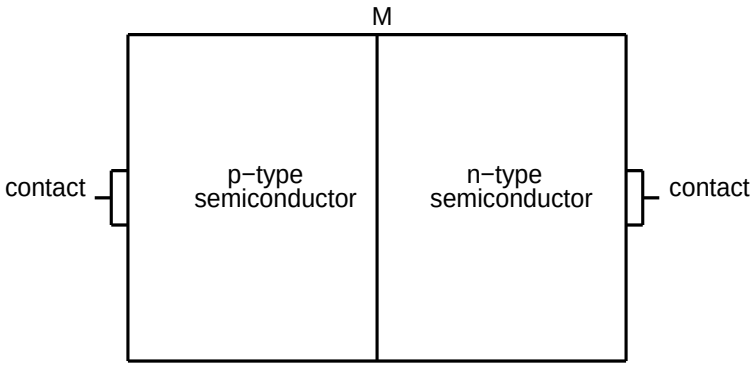

Figure 3.1: The geometric layout of a representative one-dimensional abrupt p-n junction. M denotes the metallurgical junction between the p-type and n-type regions.

of the last scattering event that the $i-th$ electron has experienced. Under the action of an applied electric field in the x-direction, assuming that the initial electron velocity of the $i-th$ electron in the x-direction is $u_x(t_i)$, the velocity of this electron in the x-direction at time t may be written as

$$v_{xi}(t) = u_{xi}(t_i) - \frac{q\mathcal{E}_x}{m_e}(t - t_i), \tag{3.1}$$

where q denotes the electron charge, m_e represents the mass of the electron, and $\mathcal{E}_x$ is the electric field in the x-direction. The drift velocity of the an electron ensemble is defined to be

$$v_{edx} \equiv \frac{[v_{x1} + v_{x2} + ... + v_{xN}]}{N}. \tag{3.2}$$

Noting that the average value of the initial velocity of the electrons over the ensemble is nil, i.e., that

$$\frac{u_{x1}(t_1) + u_{x2}(t_2) + ... + u_{xN}(t_N)}{N} = 0, \tag{3.3}$$

this drift velocity, defined in Eq. (3.2), may instead be expressed as

$$v_{edx} = \frac{-q\mathcal{E}_x}{m_e}\left[\frac{(t - t_1) + (t - t_2) + ... + (t - t_N)}{N}\right]. \tag{3.4}$$

Noting that the average free time for each electron over the ensemble, i.e., the average time between t_i to t when $i-th$ electron is free, may be expressed as

$$\overline{t - t_i} = \frac{(t - t_1) + (t - t_2) + ... + (t - t_N)}{N}, \tag{3.5}$$

it is seen that Eq. (3.4) may instead be represented as

$$v_{edx} = -\frac{q\mathcal{E}_x}{m_e}\overline{(t - t_i)}, \tag{3.6}$$

where $(\overline{t - t_i})$ corresponds to the average free time for the electrons between scattering events. Defining the electron drift mobility

$$\mu_e = \frac{q\mathcal{E}_x}{m_e}(\overline{t - t_i}), \tag{3.7}$$

it is thus seen that

$$v_{edx} = -\mu_e \mathcal{E}_x. \tag{3.8}$$

That is, the electron drift velocity scales linearly with the applied electric field in the x-direction, $\mathcal{E}_x$. A similar analysis may be employed to show that the hole drift mobility in the x-direction,

$$v_{hdx} = \mu_h \mathcal{E}_x, \tag{3.9}$$

where μ_h denotes the hole drift mobility, this mobility being defined in a similar manner to the electron drift mobility. The electron and hole drift mobilities, corresponding to c-Si and crystalline germanium (c-Ge) at 300 K, are tabulated in Table 3.1.

Table 3.1: The electron and hole drift mobilities associated with c-Si and c-Ge at 300 K [27].

Materials	μ_e (cm^2/V·s)	μ_h (cm^2/V·s)
c-Si	1400	470
c-Ge	3900	1900

The current density associated with an electric field applied in the x-direction may be expressed as the sum over the contributions due to the

electrons and holes, respectively. In particular, the current density associated with drifting electrons

$$J_{edx} = -qnv_{edx}, \tag{3.10}$$

where n denotes the electron concentration (the negative sign is introduced as electrons are negatively charged), while the current density associated with drifting holes

$$J_{hdx} = qpv_{hdx}, \tag{3.11}$$

where p represents the hole concentration. Using equations Eqs. (3.8) and (3.9), Eqs. (3.10) and (3.11) may instead be written as

$$J_{edx} = qn\mu_e\mathcal{E}_x, \tag{3.12}$$

and

$$J_{hdx} = qp\mu_h\mathcal{E}_x, \tag{3.13}$$

respectively. Thus, the total current density in the x-direction associated with drifting charge carriers,

$$J_{dx} = J_{edx} + J_{hdx}, \tag{3.14}$$

which may in turn be expressed as

$$J_{dx} = (qn\mu_e + qp\mu_h)\mathcal{E}_x. \tag{3.15}$$

In the absence of an applied electric field, charge carriers, be they electrons or holes, diffuse from regions of higher concentration to regions of lower concentration. The flux of electrons in the x-direction

$$\phi_e = -D_e\frac{\partial n}{\partial x}, \tag{3.16}$$

where D_e denotes the electron diffusion coefficient. Accordingly, as the electrons have a charge of $-q$, the current density corresponding to electron diffusion may be expressed as

$$J_{eDx} = qD_e \frac{\partial n}{\partial x}. \tag{3.17}$$

A similar analysis indicates that the flux of holes in the x-direction may be expressed as

$$\phi_{hDx} = -D_h \frac{\partial p}{\partial x}, \tag{3.18}$$

where D_h denotes the hole diffusion coefficient. Accordingly, as the holes have a charge of q, the hole current density corresponding to hole diffusion may be expressed as

$$J_{hDx} = -qD_h \frac{\partial p}{\partial x}. \tag{3.19}$$

The total current density in the x-direction associated with diffusive processes may be expressed as the sum over the contributions corresponding to the electrons and holes. Adding Eqs. (3.17) and (3.19), the diffusion current density may be expressed as

$$J_{Dx} = qD_e \frac{\partial n}{\partial x} - qD_h \frac{\partial p}{\partial x}. \tag{3.20}$$

The diffusion coefficients, corresponding to c-Si and c-Ge at 300 K, are tabulated in Table 3.2.

It is often the case that one has both an applied electric field and charge carrier concentration gradients. Accordingly, both drift and diffusion processes must be taken into account when determining the total current flux. These contributions to the overall current flux are schematically depicted

Table 3.2: The electron and hole diffusion coefficients associated with c-Si and c-Ge at 300 K [28].

Materials	D_e (cm^2/s)	D_h (cm^2/s)
c-Si	35	12
c-Ge	100	49

in Figure 3.2. To zeroth-order, these charge carrier transport processes are independent of each other, and thus, the total current may be expressed as a sum over that due to drift and that due to diffusion processes, i.e., linear superposition applies. Thus, the total current density

$$J_x = J_{dx} + J_{Dx}. \tag{3.21}$$

While equation Eq. (3.21) will not be explicitly used in the subsequent analysis, in general, it is the equation to use in cases where one has both an applied electric field and variations in the charge carrier concentrations [26].

Recombination processes between the charges play an important role in influencing the performance of devices. When semiconductors are subject to a stimulus, for example, light in the case of a photovoltaic solar cell, excess electron-hole pairs can be generated. These charge carriers also recombine. For the case of holes in an n-type semiconductor, the excess hole concentration may be expressed as $\Delta p_n \equiv p_n - p_{no}$, where p_n represents the concentration of holes in the n-type region, it being a function of position, and p_{no} denotes the equilibrium concentration in the n-type region; the p script refers to the fact that the charges considered are holes and the n subscript refers to the fact that they are in the n-type semiconductor region,

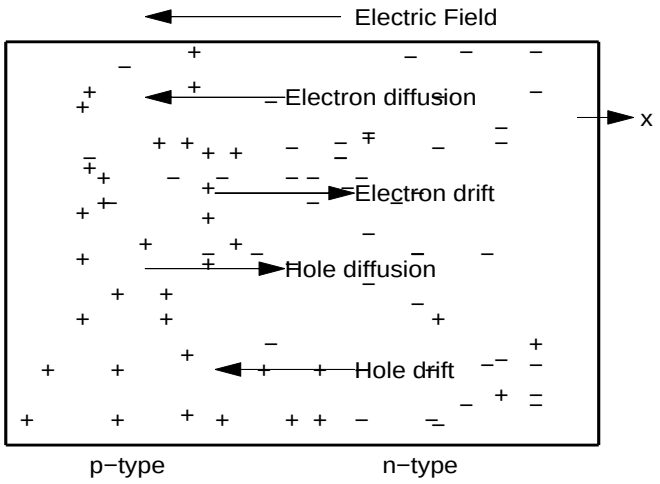

Figure 3.2: The contributions to the overall current flux attributable to the various drift and diffusion processes. It is assumed that the electric field points from right to left [26]. The p-n junction architecture has been assumed.

i.e., they are minority charge carriers.

For the case of excess holes combining with a lifetime of τ_h, the charge continuity equation in the x-direction may be expressed as

$$\frac{1}{q}\frac{\partial J_{hx}}{\partial x} = -\frac{p_n - p_{no}}{\tau_h}, \tag{3.22}$$

where this equation accounts for the rate with which charge enters a differential volume in order to compensate for the charge carrier recombination that occurs within. In the absence of an applied electric field, recalling Eq. (3.19), Eq. (3.22) reduces to

$$-D_h\frac{\partial^2 p_n}{\partial x^2} = -\frac{p_n - p_{no}}{\tau_h}, \tag{3.23}$$

which can be generalized to include a charge generation related term. For just the excess holes in the n-type semiconductor region, neglecting all variations with respect to time, this charge continuity equation reduces to

$$D_h\frac{d^2\triangle p_n}{dx^2} = \frac{\triangle p_n}{\tau_h}. \tag{3.24}$$

Defining the hole diffusion length, $L_h \equiv \sqrt{D_h\tau_h}$, Eq. (3.24) may alternatively be expressed as

$$\frac{d^2\triangle p_n}{dx^2} = \frac{\triangle p_n}{{L_h}^2}. \tag{3.25}$$

A similar expression may be determined for the excess electrons in the p-type semiconductor region, i.e.,

$$\frac{d^2\triangle n_p}{dx^2} = \frac{\triangle n_p}{{L_e}^2}, \tag{3.26}$$

where $L_e \equiv \sqrt{D_e\tau_e}$ is referred to as the electron diffusion length and $\Delta n_p \equiv n_p - n_{po}$, n_p representing the concentration of electrons in the p-type region,

it being a function of position, and n_{po} denotes the equilibrium concentration of electrons in the p-type region; the n script refers to the fact that the charges considered are electrons and the p subscript refers to the fact that they are in the p-type semiconductor region, i.e., they are minority charge carriers. The electron and hole diffusion lengths, L_e and L_h, respectively, corresponding to c-Si and c-Ge at 300 K, are tabulated in Table 3.3. These diffusion lengths will be used in the subsequent analysis. These equations, i.e., Eqs. (3.25) and (3.26), are generally referred to as the ambipolar diffusion equations.

Table 3.3: The electron and hole diffusion lengths associated with c-Si and c-Ge at 300 K [26].

Materials	L_e (μm)	L_h (μm)
c-Si	41	24
c-Ge	79	48

3.4 The p-n junction with no applied bias

It is instructive to consider the distribution of charges within a one-dimensional abrupt p-n junction, as shown in Figure 3.3. The p-type semiconductor region is doped with acceptors. As a result, at normal operating temperatures, i.e., when the acceptors are fully ionized, these acceptors will be negatively charged and the corresponding bulk semiconductor will possess a surplus of holes, i.e., its polarity will be p-type. Similarly, the n-type semiconductor region is doped with donors. As a result, at normal operat-

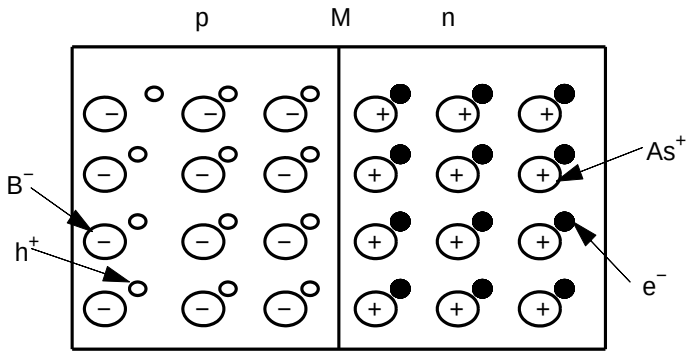

Figure 3.3: The distribution of charges within a one dimensional abrupt p-n junction.

ing temperatures, i.e., when the donors are fully ionized, these donors will be positively charged and the bulk semiconductor will posses a surplus of electrons, i.e., its polarity will be n-type. It should noted that while the acceptors and donors atoms are fixed in their position, i.e., effectively they are immobile, the electrons and holes are free to transit within the material [26].

As the p-type region of the semiconductor has a high hole concentration, these holes tend to diffuse towards the n-type region. Similarly, as the n-type region of the semiconductor has a high electron concentration, these electrons tend to diffuse towards the p-type region. Holes that diffuse into the n-type region will recombine with the electrons in this region near the junction. Similarly, electrons that diffuse into the p-type region will recombine with the holes in this region near the junction. As a result, the junction region becomes depleted of free charge carriers when contrasted with the bulk p-type and n-type regions far from the junction; see Figure 3.4 in which the distribution of spatially distributed charge is depicted. Thus, a space-charge region exists around the junction, comprised of a positive distribution of charge on the n-type semiconductor side and a negative distribution of charge on the p-type semiconductor side, these charge distributions corresponding to the immobile dopant atoms, i.e, ions, be they acceptors or donors.

This space-charge region will create an internal "built-in" electric field that points from the n-type region to the p-type region; see Figures 3.4, and 3.5. This electric field acts to drift holes back into the p-type region and drift electrons back into the n-type region. The greater the amount of

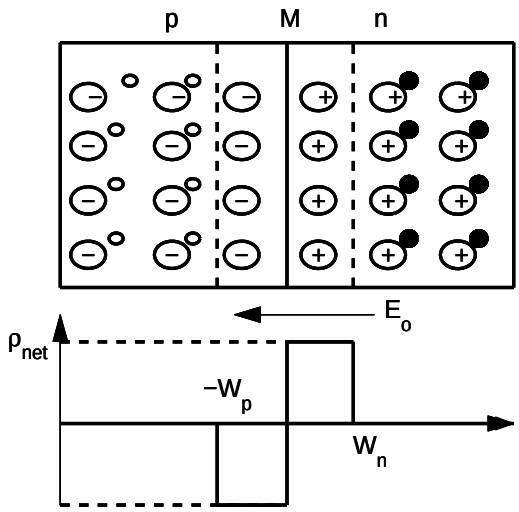

Figure 3.4: The depletion region formed in a p-n junction under no bias. The net distributed charge, ρ_{net}, is also indicated. E_0 denotes the "built-in" electric field.

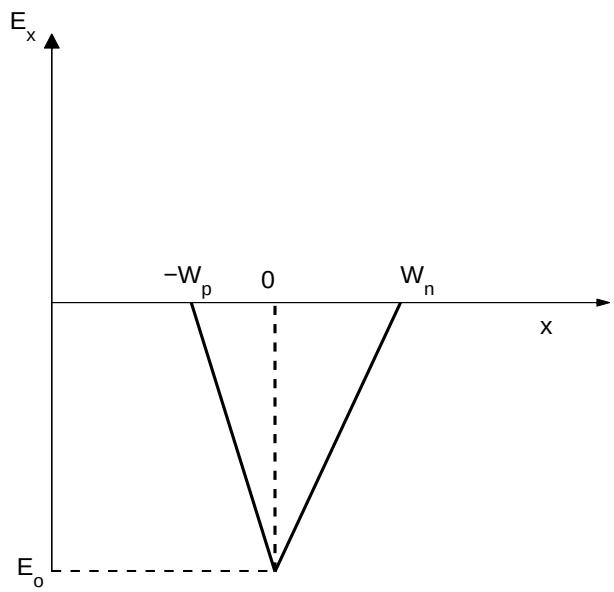

Figure 3.5: The electric field within a p-n junction under no bias. The electric field points from right to left, $x = -W_p$ and $x = W_n$ denoting the space-charge/neutral region boundaries for the p-type and n-type regions, respectively [26].

charge that is separated between these regions, the greater the "built-in" electric field. When equilibrium is established, the flux of charge carriers attributed to diffusion is exactly compensated by that due to drift, both for electrons and for holes. Thus, under equilibrium conditions, an electric potential profile, corresponding to the p-n junction, will exist. This potential profile modifies the band diagram associated with this semiconductor device. This potential profile is depicted in Figure 3.6.

For a p-n junction under zero bias, the Fermi energy level, E_F, remains constant. To determine the band diagram corresponding to such a junction, it is noted that the position of the electron energy levels change according to the relative value of the potential. The resultant band diagram is depicted in Figure 3.7. Note that in the bulk p-type region, i.e., far from the junction, holes are the dominant charge carriers as the Fermi energy level is close to the valence band edge [29]. In contrast, it is noted that in the bulk n-type region, i.e., far from the junction, electrons are the dominant charge carriers as the Fermi energy level is close to the conduction band edge. Across the junction, the charge carrier concentrations change according to the position of the band edges with respect to the Fermi energy level. The dependence of the charge carrier concentrations on the position within the p-n junction is depicted in Figure 3.8.

The bulk concentrations of the electrons and holes in the n-type region under no bias may be written as n_{no} and p_{no}, respectively, where the subscript "o" refers to the case of no bias. The bulk concentrations of the electrons and holes in the p-type region under no bias may be written as n_{po} and p_{po}, respectively. Assuming that all the donors and acceptors are

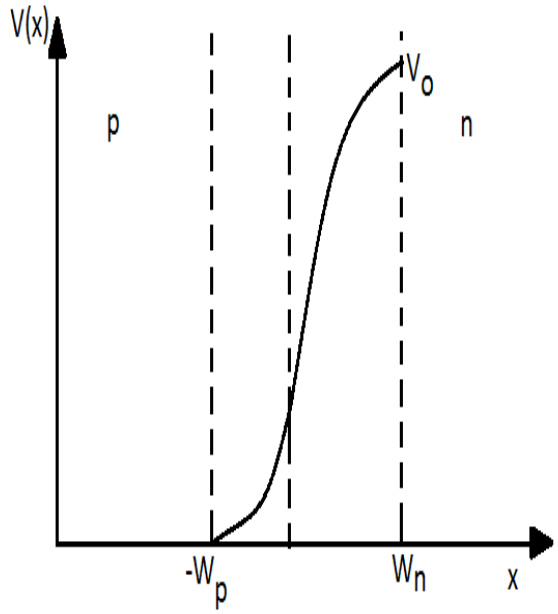

Figure 3.6: The electric field corresponding to a p-n junction under no bias. V_o denotes the "built-in" potential.

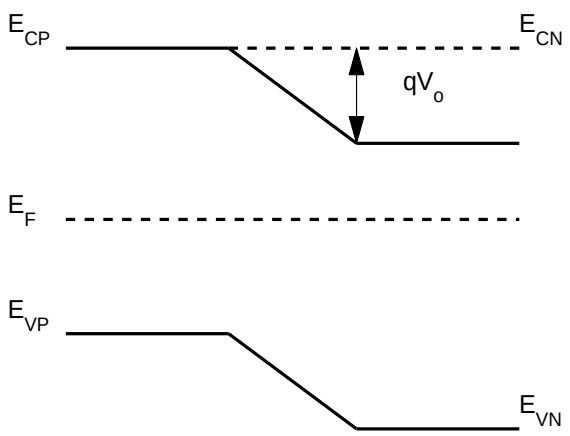

Figure 3.7: The energy band diagram of an unbiased p-n junction [29].

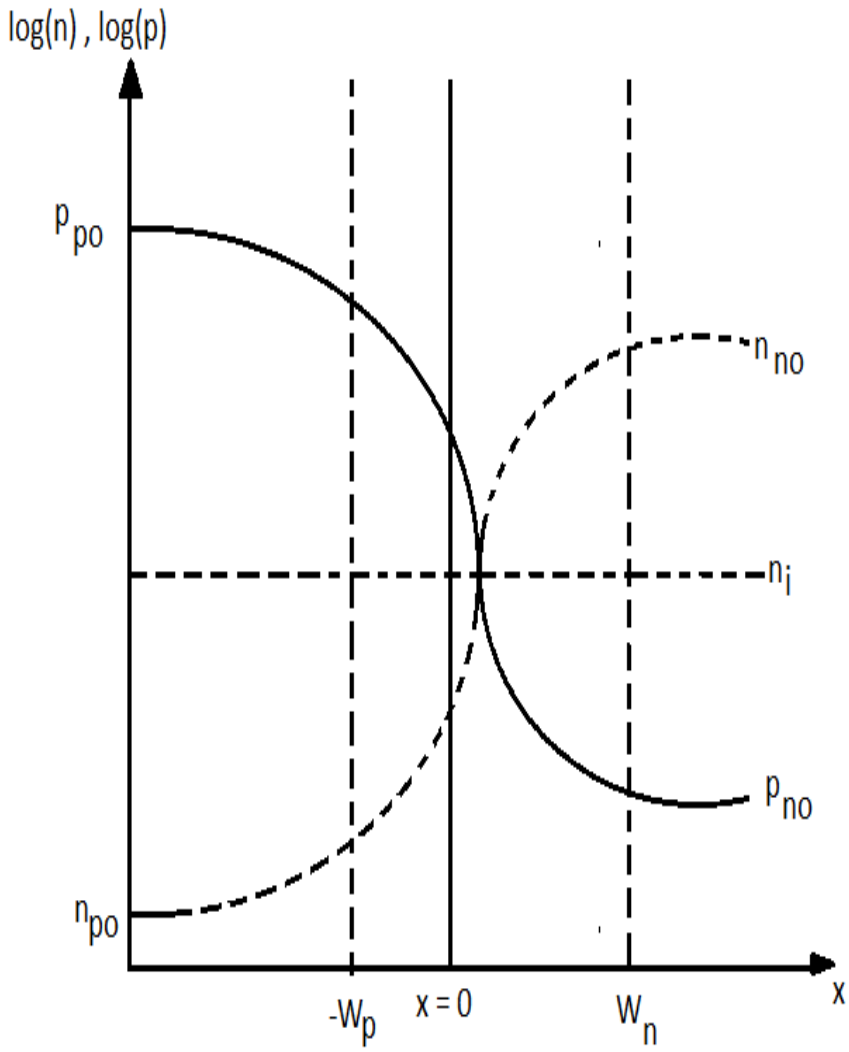

Figure 3.8: The charge carrier concentrations as a function of the position within the p-n junction.

completely ionized, the "built-in" potential,

$$V_o = \frac{kT}{q} \ln\left(\frac{p_{po} n_{no}}{n_i^2}\right), \tag{3.27}$$

where n_i denotes the intrinsic charge carrier concentration. Noting that in equilibrium

$$pn = n_i^2, \tag{3.28}$$

it is seen that in the bulk of the n-type region,

$$p_{no} n_{no} = n_i^2, \tag{3.29}$$

and that in the bulk of the p-type region,

$$p_{po} n_{po} = n_i^2. \tag{3.30}$$

This suggests that Eq. (3.27) may instead be written as

$$V_o = \frac{kT}{q} \ln\left(\frac{p_{po} n_{no}}{p_{no} n_{no}}\right), \tag{3.31}$$

using Eq. (3.29). Thus, it can be shown that,

$$p_{no} = p_{po} \exp\left(-\frac{qV_o}{kT}\right). \tag{3.32}$$

Alternately, Eq. (3.27) may be rewritten as

$$V_o = \frac{kT}{q} \ln\left(\frac{p_{po} n_{no}}{p_{po} n_{po}}\right), \tag{3.33}$$

using Eq. (3.30). Thus,

$$n_{po} = n_{no} \exp\left(-\frac{qV_o}{kT}\right). \tag{3.34}$$

These expressions relate the minority charge carriers concentrations on one side of the junction with the correspond majority charge carrier concentrations on the other side of the junction.

3.5 The p-n junction under forward-bias

When a positive potential is applied across the terminals of a p-n junction, i.e., when the p-n junction is under forward bias, the equilibrium that was established between the drift and diffusion components of the current density for the no bias case is disrupted. As a result, there will now be an injection of excess minority charge carriers across the junction, i.e., excess holes will be injected into the n-type region and excess electrons will be injected into the p-type region. This will lead to a net current across the device. With a positive potential across the p-n junction, the "built-in" potential reduces from V_o to $V_o - V$, where V denotes the amount by which the p-n junction is forward biased. As a consequence, the band diagram is modified from the no bias case, as is seen in Figure 3.9. Under forward bias, the Fermi energy level is no longer constant. Instead, it changes according to the applied voltage, V, this also being shown in Figure 3.9. As a result, there is a reduction in the height of the barrier [26] and a corresponding reduction in the width of space-charge region [29]; see Figure 3.10. Accordingly, the expressions for the minority charge carrier concentrations are modified from those determined for the zero-bias case, i.e., Eqs. (3.32) and (3.34).

An injection of minority charge carriers across the junction under the action of a forward bias will lead to minority charge carrier concentrations that greatly exceed their corresponding steady-state values. These minority charge carriers will recombine as they diffuse into the neutral regions, i.e., away from the space-charge region. Thus, the ambipolar diffusion equations defined in Section 3.3, i.e., Eqs. (3.25) and (3.26), may be used to determine

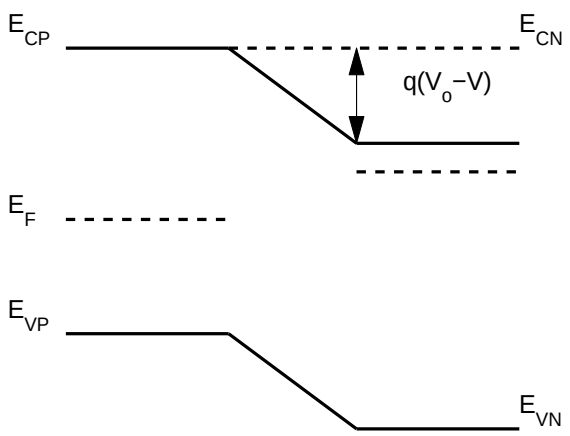

Figure 3.9: The energy band diagram of a forward-biased p-n junction [29].

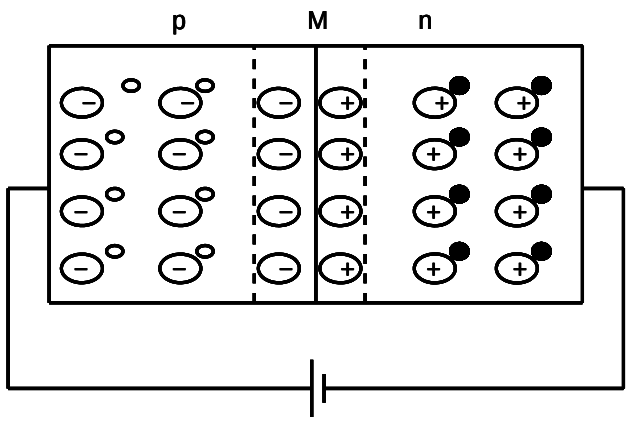

Figure 3.10: Depletion region formed in a p-n junction under forward bias. Note that the space-charge region is narrower than for the no bias case.

the profile of excess minority charge carrier concentrations. Considering Figure 3.11, the excess hole concentration in the n-type region may be shown to be

$$\Delta p_n = p_n(x = W_n) \exp\left(-\frac{(x - W_n)}{L_h}\right), \tag{3.35}$$

where it has been assumed that the n-type neutral region is long and where $p_n(x = W_n)$ is the boundary condition at the space-charge/neutral region boundary on the n-type side, this being determined by the charge carrier injection. Similarly, the excess electron concentration in the p-type region may be shown to be

$$\Delta n_p = n_p(x = -W_p) \exp\left(\frac{(x + W_p)}{L_e}\right), \tag{3.36}$$

where it has been assumed that the p-type neutral region is long and where $n_p(x = -W_p)$ is the boundary condition at the space-charge/neutral region boundary on the p-type side, this being determined by charge carrier injection.

The amount by which excess minority charge carriers are injected into a region is related to the reduction in the barrier height, V. Specifically, it may be shown that

$$\Delta p_n(x = W_n) = p_{no}\left[\exp\left(\frac{qV}{kT}\right) - 1\right], \tag{3.37}$$

and that

$$\Delta n_p(x = -W_p) = n_{po}\left[\exp\left(\frac{qV}{kT}\right) - 1\right], \tag{3.38}$$

where the total minority charge carrier concentration may be determined by adding the corresponding equilibrium charge carrier concentrations, i.e., p_{no} for the case of holes in the n-type region and n_{po} for the case of electrons in

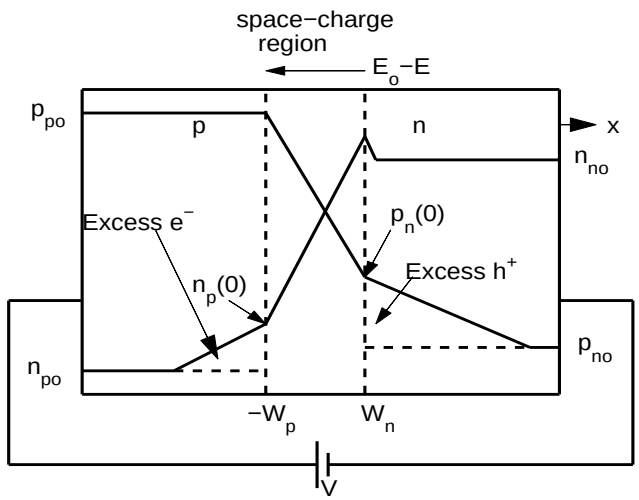

Figure 3.11: The excess hole and electron concentrations in a p-n junction Eqs. (3.37) and (3.38) establish the boundary conditions. The $x = -W_p$ represents the location of the space-charge/neutral region boundary in the p-type region of junction. The $x = W_n$ represents the location of the space-charge/neutral region boundary in the n-type region of junction.

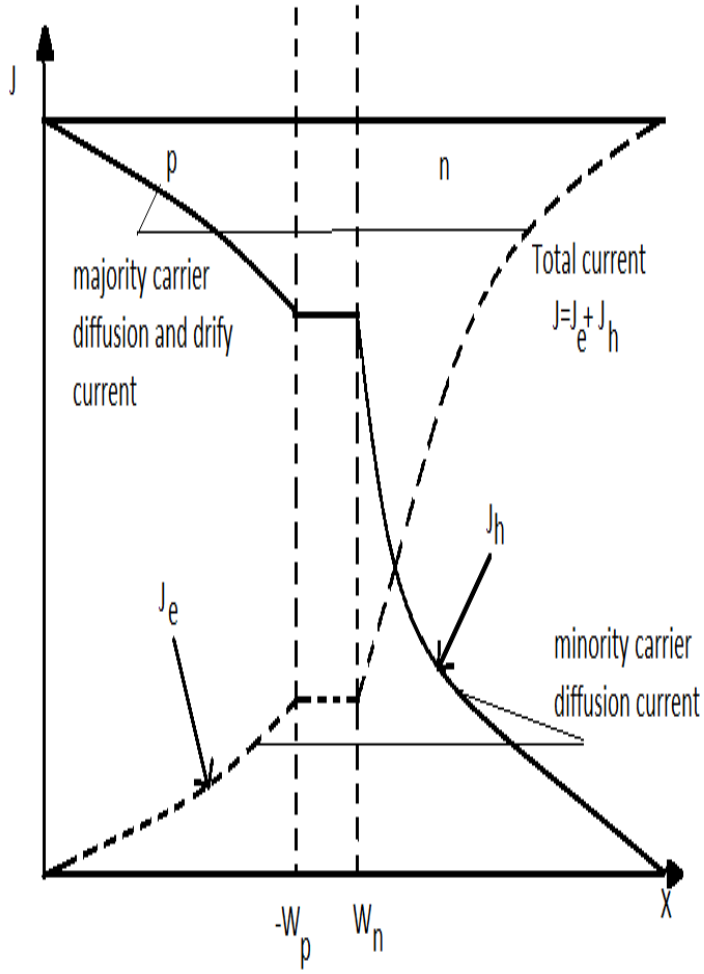

Figure 3.12: The contributions to the current density associated with the drift and diffusion processes.

the p-type region.

From Section 3.3, it was demonstrated the total current density is determined by the sum over that due to drift and diffusion processes, their being four possible current components contributing to the overall current density; recall Figure 3.12. It can be shown that the drift and diffusion current densities associated with the majority charge carriers are negligible at the edges space-charge/neutral region boundaries; see Figure 3.12. Accordingly, the current density may be determined by evaluating the sum over the hole and electron diffusion current densities at the different space charge/neutral region boundaries for each minority charge carrier considered. That is

$$J = J_{hDx}|_{x=+W_n} + J_{eDx}|_{x=-W_p}, \tag{3.39}$$

where $J_{hDx}|_{x=+W_n}$ refers to the hole diffusion current on the n-type semiconductor side, i.e., evaluated at $x = +W_n$, and $J_{eDx}|_{x=-W_p}$, i.e., evaluated at $x = -W_p$, represents the electron diffusion current on the p-type semiconductor side. Thus, from Eqs. (3.37) and (3.38), and using Eqs. (3.17) and (3.19), it can be shown that

$$J = \left(\frac{qD_h}{L_h n_{no}} + \frac{qD_e}{L_e p_{po}}\right) n_i^2 \left[\exp\left(\frac{qV}{kT}\right) - 1\right]. \tag{3.40}$$

This expression for the current density may alternatively be expressed as

$$J = J_{so}\left[\exp\left(\frac{qV}{kT}\right) - 1\right], \tag{3.41}$$

where all the terms have been defined previously, the scale current density,

$$J_{so} = \left(\frac{qD_h}{L_h n_{no}} + \frac{qD_e}{L_e p_{po}}\right) n_i^2. \tag{3.42}$$

Eqs. (3.40) is referred to as the ideal diode current-voltage device characteristic associated with a p-n junction, i.e., a p-n junction without recombination processes. The corresponding current may be obtained by multiplying the current density with the area of the junction.

3.6 The p-n junction under reverse bias

When a negative potential is applied across the terminals of a p-n junction, i.e., when the p-n junction is under reverse bias, the electric field related to the voltage across the terminals is in the same direction as that related to the "built-in" electric field, as can be seen from Figure 3.13. As a result, the potential barrier is increased and the current across the p-n junction becomes negligible. In addition, the breadth of the space-charge region becomes wider [29]. The resultant band diagram is depicted in Figure 3.14.

3.7 Recombination processes

In the event that the charge carriers recombine, these recombining charge carriers must be supplied by the external current. An elementary model for these recombination processes may be obtained by plotting the electron and hole concentrations across the space charge region, as is shown in Figure 3.15. If the mean hole recombination time associated with the n-type region of the space-charge region is denoted τ_h and the mean electron recombination time associated with the p-type region of the space-charge region is denoted τ_e, assuming a thick space-charge region, then the recombination current density may be expressed as

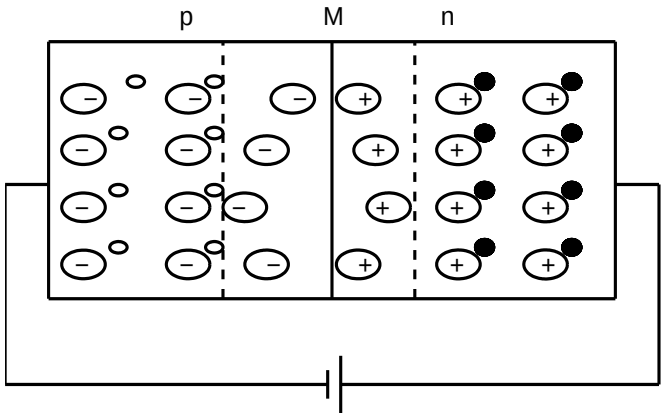

Figure 3.13: Depletion region formed in a p-n junction under reverse bias. Note that the space-charge region is wider than for the no bias case.

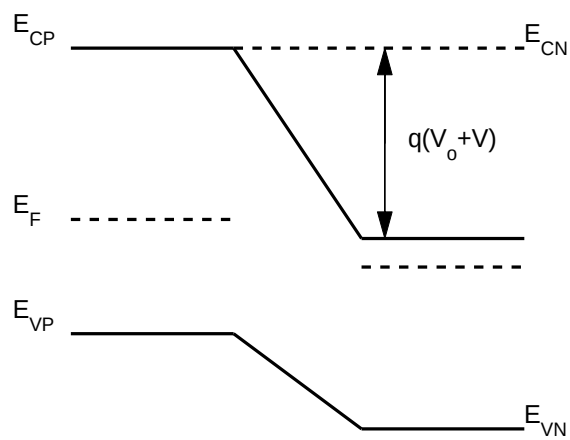

Figure 3.14: The energy band diagram for a reverse-biased p-n junction [29].

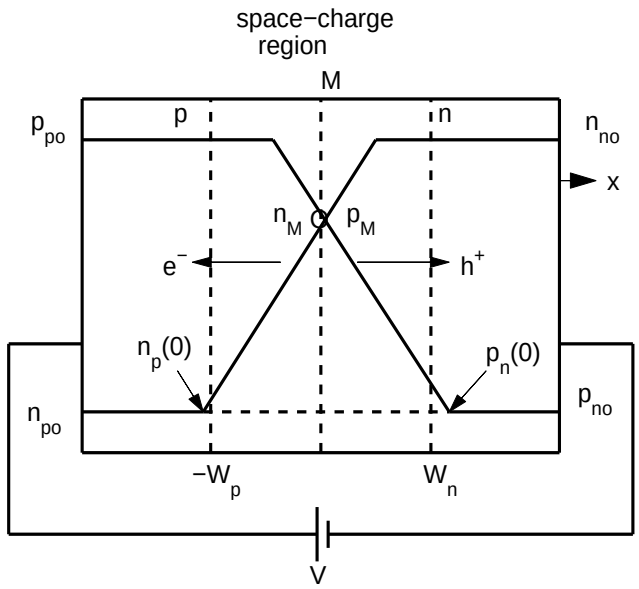

Figure 3.15: The injection of charge carriers and the recombination within the space-charge region.

$$J_{recom} = \frac{q\frac{1}{2}W_p n_M}{\tau_e} + \frac{q\frac{1}{2}W_n p_M}{\tau_h}, \tag{3.43}$$

where n_M and p_M are the concentrations of electrons and holes at center of the junction, respectively; see Figure 3.15. Assuming that the junction is symmetric in form, it may be shown that

$$p_M = n_M = n_i \exp\left(\frac{qV}{2kT}\right). \tag{3.44}$$

Thus, the current density due to recombination may be expressed as

$$J_{recom} = q\frac{1}{2}W_p\left(\frac{1}{\tau_e} + \frac{1}{\tau_h}\right)\exp\left(\frac{qV}{2kT}\right). \tag{3.45}$$

This expression for the current density may alternatively be expressed as

$$J_{recom} = J_{ro}\exp\left(\frac{qV}{2kT}\right), \tag{3.46}$$

where the recombination scale current

$$J_{ro} = q\frac{1}{2}W_p\left(\frac{1}{\tau_e} + \frac{1}{\tau_h}\right). \tag{3.47}$$

With recombination processes taken into account, within the framework of linear superposition, the overall current density may be expressed as

$$J(v) = J_{so}\exp\left(\frac{qV}{kT}\right) + J_{ro}\exp\left(\frac{qV}{2kT}\right), \tag{3.48}$$

where the first term represents the current density related to the ideal diode and the second term denotes the current density contribution attributable to recombination processes. These contributions to the current density are plotted as a function of the applied voltage in Figure 3.16, for the case of J_{so} set to 1 μA/cm^2 and J_{ro} set to 10 nA/cm^2, these being representative values

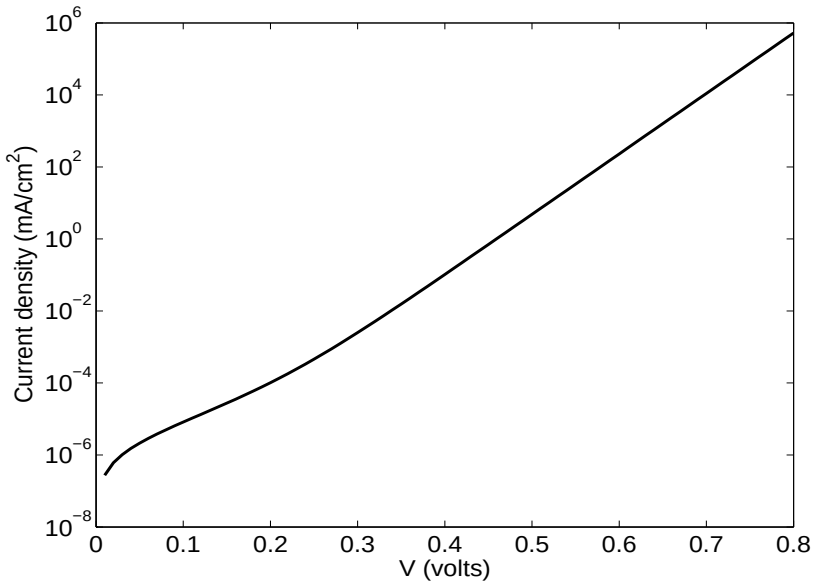

Figure 3.16: The current density-voltage device characteristics corresponding to Eq. (3.48) with J_{so} set to 1 μA/cm^2 and J_{ro} set to 10 nA/cm^2. The temperature is set to 300 K.

found in the literature. The impact that recombination processes play in determining the performance of a photovoltaic solar cell will be investigated further in Chapter 4 using this expression.

It is often the case that the current-voltage device characteristic associated with a p-n junction may be represented using the simple empirical relationship

$$J(v) = J_o\left[\exp\left(\frac{qV}{\eta kT}\right) - 1\right], \tag{3.49}$$

where η denotes the ideality factor. The ideality factor, η, represents the amount of recombination that occurs. A value of η set to 2 implies that recombination processes dominate, while a value of η set to unity suggests that recombination processes play a negligible role. For the purposes of the subsequent analysis, owing to its simplicity, Eq. (3.49) will initially be employed. Later, as the impact of recombination processes are further examined, Eq. (3.48) will be used instead.

Chapter 4

Solar cell performance analysis

4.1 Motivation

Fundamentally, a photovoltaic solar cell is created when a p-n junction is exposed to light. The photons in the light generate electron-hole pairs within the junction. These pairs are then separated by the large "built-in" electric field that occurs at the p-n interface within such a junction. The transport of charge carriers, be they electrons or holes, creates a current. As the incident light that the p-n junction receives is directly responsible for this current, within the context of a solar cell device application, such a current is usually referred to as a photocurrent. It is the product of the photocurrent and the voltage developed across the terminals of such a p-n junction that allows for power to be delivered to a load from the solar cell.

Following Prince [30], the behavior of a solar cell may be modeled as a p-n junction in parallel with a solar flux controlled current source. The corresponding circuit model is depicted in Figure 4.1. Clearly, a detailed understanding of p-n junction operation is crucial to the understanding of the behavior of this circuit. The functioning of the solar flux controlled

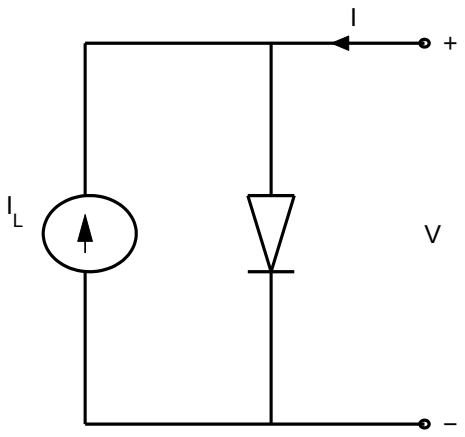

Figure 4.1: Model for the behavior of a photovoltaic solar cell. The p-n junction is in parallel with a solar flux controlled current source. This circuit model follows the suggestion of Prince [30].

current source, which in turn depends upon how the materials within the p-n junction respond to light, is also important. Linking this response to the corresponding solar spectrum is a key focus of this analysis. With the characteristics of the p-n junction established, and the operation of the solar flux controlled current source determined, the performance of such a solar cell may be assessed.

This chapter is organized in the following manner. In Section 4.2, the geometries commonly employed for photovoltaic solar cells are reviewed. Then, in Section 4.3, the overall form of the behavior of such a cell is discussed. Performance metrics, corresponding to the photovoltaic solar cell, are then introduced in Section 4.4. Following the approach of Prince [30], using an empirical model for the current-voltage p-n junction device characteristic, i.e., Eq. (3.49), the performance of a photovoltaic solar cell is examined in Section 4.5. This analysis demonstrates a shortcoming of Eq. (3.49), where the ideality factor, η, is set to values beyond unity. The relationship with the underlying material parameters corresponding to these photovoltaic solar cells is then discussed in Section 4.6. In Section 4.7, the impact that parasitic resistances have upon the performance of a photovoltaic solar cell are then presented. The relationship between this performance and the solar spectrum are then examined in Section 4.8, the dependence of the efficiency of the solar cell on the energy gap of the material being determined for the different solar spectra considered in this analysis. Finally, using a more rigorous approach, how recombination processes impact upon the performance of a photovoltaic solar cell is considered in Section 4.9.

4.2 Solar cell geometries

There have been a number of different geometries proposed for the photovoltaic solar cell. Fundamentally, all of these configurations are in the form of a p-n junction. A p-n junction is comprised of a p-type semiconductor region abutted against an n-type semiconductor region. It is the minority charge carriers in either region that determine the photovoltaic response of such a junction. As the electrons within c-Si have a greater mobility than the holes (recall Table 3.1), thicker p-type regions are preferred, i.e, electrons are the minority charge carrier within the p-type c-Si region. Accordingly, most modern c-Si based photovoltaic solar cells are comprised of a thin n-type c-Si layer and a thicker p-type c-Si layer. A representative one-dimensional p-n junction, that may be used for photovoltaic solar cell device applications, is depicted in Figure 4.2. Real photovoltaic solar cell geometries will be more complex, of course.

Multidimensional photovoltaic solar cells have been introduced in order to achieve greater efficiencies. Lately, for example, Kayes and Atwater have proposed a distribution of radial p-n junctions [31]. Kayes and Atwater found that the efficiencies produced from these radial p-n junctions are higher than those corresponding to conventional p-n junctions; this is true for low lifetime materials [31]. Radial p-n junctions offer a greater p-n junction interface surface area. Fundamentally, it is this greater surface area that is responsible for these greater efficiencies.

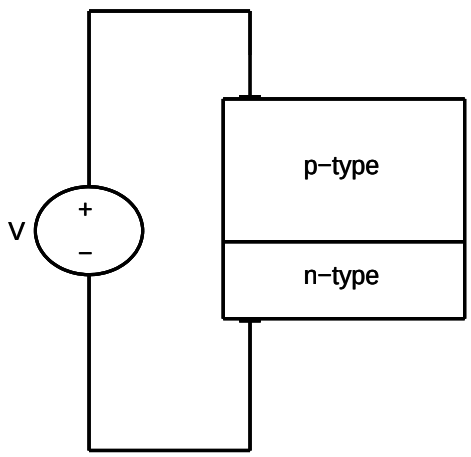

Figure 4.2: A representative one dimensional p-n junction that may be used for photovoltaic device applications. Note that the p-type layer is thicker than the n-type layer.

4.3 Photovoltaic solar cell behavior

For the circuit model depicted in Figure 4.1, the photovoltaic solar cell behaves as a battery. Under light illumination, the corresponding photon flux generates electron-hole pairs within the semiconductor. The large electric field that exists at the interface between the p-type and n-type regions separates these charge carriers, and they drift under the action of the applied electric field, leading to a photocurrent. The separation of charges that occurs leads to the development of a potential difference across the terminals of the p-n junction, i.e., a photovoltage. This effect is referred to as the photovoltaic effect, and it is found in a variety of natural and engineered structures. It is what is responsible for the behavior of the photovoltaic solar cell.

4.4 Photovoltaic solar cell performance metrics

In Figure 4.3, a representative current-voltage device characteristic associated with a photovoltaic solar cell is depicted. There are three important performance metrics associated with this current-voltage device characteristic: (1) the open-circuit voltage, V_{oc}, (2) the short-circuit current, I_{sc}, and (3) the fill-factor associated with the device, FF. Two of these metrics are depicted in Figure 4.3. The open-circuit voltage, V_{oc}, corresponds to the voltage that exists across the solar cell when no current flows. The short-circuit current, I_{sc}, corresponds to the current that emerges from the solar cell circuit when the voltage across the solar cell is set exactly to zero. The fill-factor, FF, corresponds to the maximum power that may be delivered

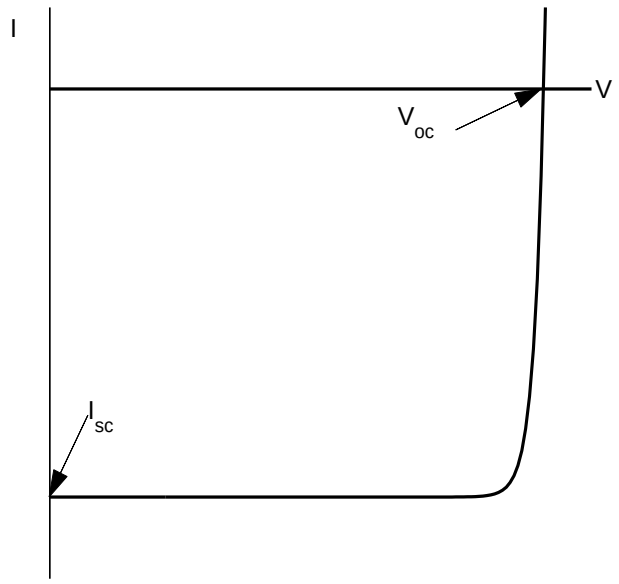

Figure 4.3: A representative current-voltage device characteristic associated with a photovoltaic solar cell.

to an external load divided by the product of V_{oc} and I_{sc}, i.e.,

$$FF \equiv \frac{P_{max}}{V_{oc} I_{sc}}, \tag{4.1}$$

where P_{max} denotes this maximum power. Essentially, the fill-factor provides a measure as to how rounded the current-voltage device characteristic of the photovoltaic solar cell is, a fill-factor of unity corresponding to a completely abrupt current-voltage device characteristic. In Figure 4.4, the current-voltage device characteristics, corresponding to a variety of fill-factor selections, is depicted.

Thus far, the focus of the analysis related to the current-voltage device characteristics associated with a photovoltaic solar cell has centered on the fourth quadrant. This is the region of the current-voltage device characteristic over which power may be delivered from the photovoltaic solar cell to an external load. Through a reversal in the polarity of the current, however, this fourth quadrant may be mapped into the first quadrant. This representation is often used in the characterization of the current-voltage device characteristics associated with a photovoltaic solar cell. For the purposes of this particular analysis, however, the fourth quadrant representation of the current-voltage device characteristics will be employed instead.

4.5 Photovoltaic solar cell device modeling

For the purposes of this analysis, the approach of Prince is adopted [30], the current-voltage device characteristics associated with a p-n junction being added to the current-voltage device characteristics of the solar flux controlled current source; recall Figure 4.1. The total current that is delivered

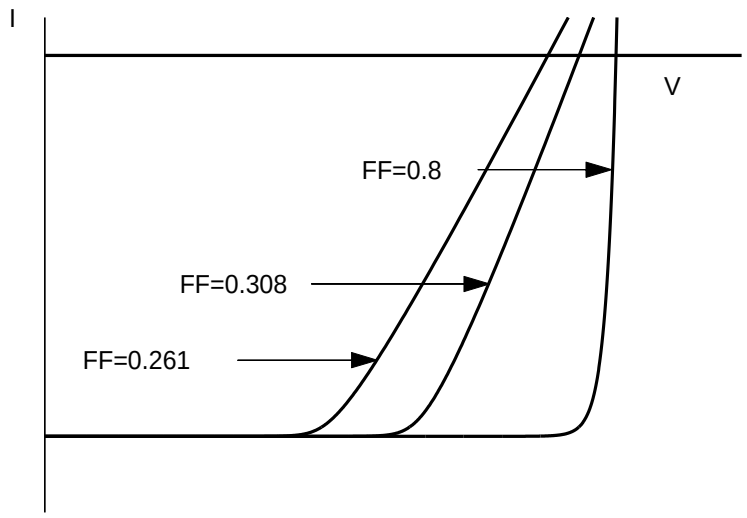

Figure 4.4: Representative current-voltage device characteristics associated with a photovoltaic solar cell for various fill-factor selections.

across the terminals of the p-n junction is thus the sum over these two contributions. This is the manner in which the current-voltage device characteristics associated with a photovoltaic solar cell will be modeled.

As was discussed in Section 3.7, the current-voltage device characteristic associated with a p-n junction may be empirically expressed as

$$I(v) = I_0 \left[\exp\left(qv/\eta kT\right) - 1\right], \tag{4.2}$$

where I represents the current, v is the voltage applied across the terminals, I_0 denotes the scale current, q is the charge of the electron, k is the Boltzmann constant, T is the temperature, and η is the ideality factor. The ideality factor, η, lies between 1 and 2 depending on the amount of recombination that occurs within the junction. When the solar-flux controlled current source is added to the mix, the resultant current-voltage device characteristic becomes

$$I(v) = I_0 \left[\exp\left(qv/\eta kT\right) - 1\right] - I_L, \tag{4.3}$$

where I_L denotes the photocurrent. Note that I_L is in the opposite direction of the dark current. This occurs as the "built-in" electric field points in the opposite direction to the forward bias direction; recall Figure 4.1.

From Eq. (4.3), it can be shown that the open-circuit voltage,

$$V_{oc} = \frac{\eta kT}{q} \ln\left(\frac{I_L}{I_o} + 1\right); \tag{4.4}$$

this may be shown by setting the $I(v)$ in Eq. (4.3) to nil. In Figure 4.5, the open-circuit voltage, V_{oc}, is plotted as a function of the ratio, $\frac{I_L}{I_o}$, for the case of η set to unity, i.e., the ideal case with no recombination. V_{oc} is normalized with respect to the thermal voltage, $\frac{kT}{q}$, for the purposes of

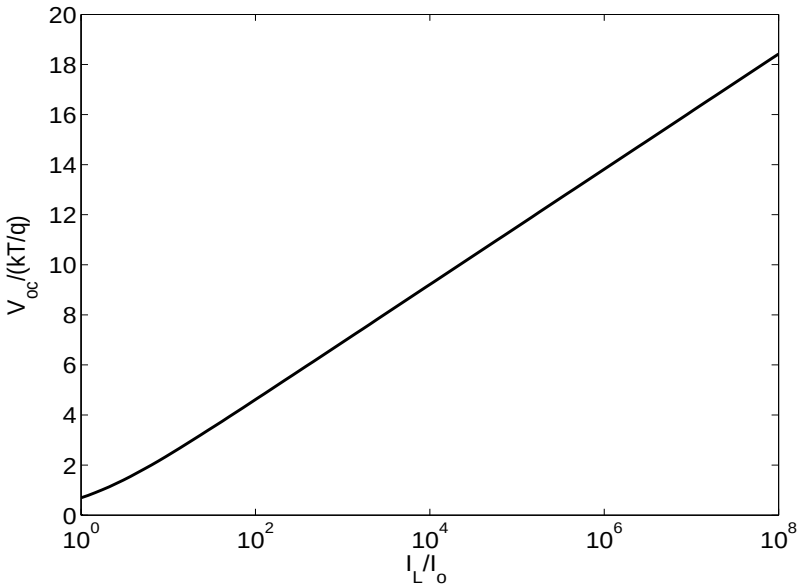

Figure 4.5: The open-circuit voltage, V_{oc}, scaled by the thermal voltage, $\frac{kT}{q}$, as a function of the ratio, $\frac{I_L}{I_o}$, for the ideality factor, η, set to unity.

this plot. It is seen that the open-circuit voltage, V_{oc}, logarithmically scales with the current produced by the solar flux controlled current source. For the special case of I_o set to 10^{-9} A, a value that is representative of the case of c-Si, the dependence of the open-circuit voltage on the photocurrent, I_L, is depicted in Figure 4.6, for two selections of η. The temperature is set to 300 K for all cases, 300 K being representative of room temperature. It is seen that for a fixed photocurrent, the open-circuit voltage, V_{oc}, scales linearly (for the temperature being set to 300 K, i.e., room temperature) with the ideality factor, η. For I_L set to 100 mA, this being a representative photocurrent value, V_{oc} varies between 0.42 and 0.84 V when η is increased from unity to two. These values are representative of those found in the literature.

The short-circuit current may be obtained by setting the voltage across the p-n junction terminals to be zero. Using Eq. (4.3), it may be shown that

$$I_{sc} = I_L; \tag{4.5}$$

this is determined by setting $v = 0$ and taking the absolute magnitude of the resultant current; recall Figure 4.3. That is, the short current corresponds to that provided from the solar flux controlled current source.

Within the framework of the elementary model for the p-n junction device characteristics that has been discussed thus far, i.e., Eq. (4.3), the power delivered from the photovoltaic solar cell to an external load,

$$p(v) = -I(v)v. \tag{4.6}$$

This power may be plotted as a function of the voltage applied across the terminals of the p-n junction, v, the negative sign allowing one to determine

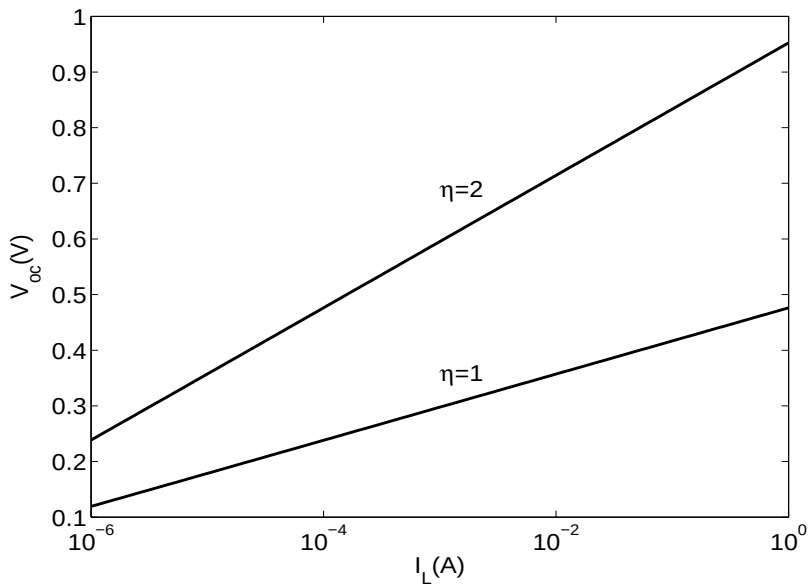

Figure 4.6: The open circuit voltage, V_{oc}, as a function of photocurrent, I_L. I_o is set to 10^{-9} A for the purposes of this analysis. Two selections of η are considered. The temperature is set to 300 K for the purposes of this analysis.

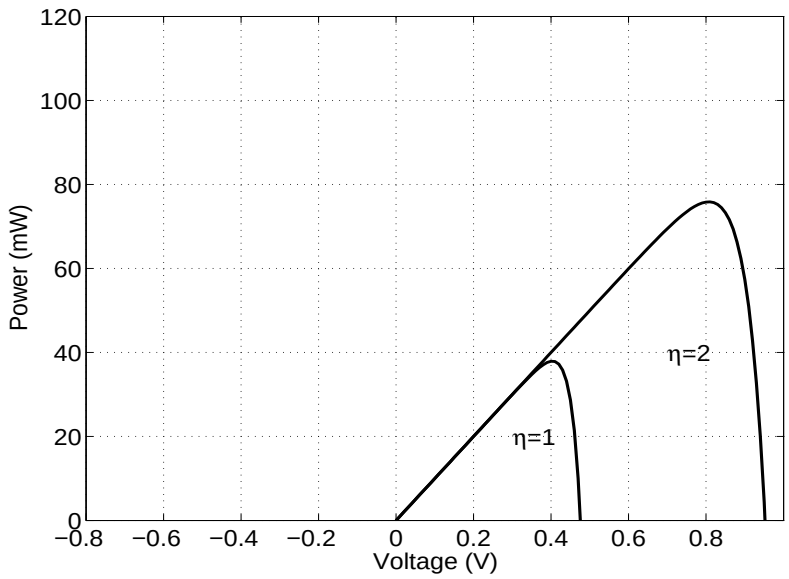

Figure 4.7: The power delivered to an external load as a function of the applied voltage for two selections of the ideality factor, η. For the purposes of this analysis, I_o is set to 10^{-9} A and I_L is set to 100 mA. The temperature is set to 300 K for all cases.

the delivered power as opposed to the absorbed power. For the case of I_o set to 10^{-9} A and I_L set to 100 mA, the resultant power delivered to an external load is plotted as a function of the applied voltage, v, in Figure 4.7, for the temperature set to 300 K; two η selections are considered, $\eta = 1$ and $\eta = 2$. For the case of η set to unity, it is seen that the power delivered to the external load becomes a maximum when the applied voltage is around 0.4 V, the maximum power delivered being around 37 mW. The corresponding fill-factor, FF, is seen to be 0.7928, i.e., ∼79.3 %. For the case η set to 2, however, it is seen that the power delivered to the external load becomes a maximum when the applied voltage is around 0.8 V, the maximum power delivered being around 75 mW. The corresponding fill-factor, FF, is seen to be 0.7940 for this case, i.e., ∼79.4 %. It is interesting to note that in this case, a greater ideality factor, i.e., more recombination, results in a slightly higher fill-factor.

In order to examine the role that the ideality factor, η, plays in influencing the fill-factor, FF, in Figure 4.8 the fill-factor is plotted as a function of I_L for the cases of η set to unity and η set to 2. For all cases, I_o is set to 10^{-9} A and the temperature is set to 300 K. The approach employed in Figure 4.7 is used to determine the corresponding fill-factor, FF. It is noted that the fill-factor increases monotonically with the photocurrent, I_L, for all cases. In addition, it is noted that results for the fill-factor corresponding to η set to 2 form an upperbound to that determined for η set to unity. This was confirms the trend that was observed earlier for the specific case of I_L set to 100 mA.

It is interesting to note that greater recombination seems to produce

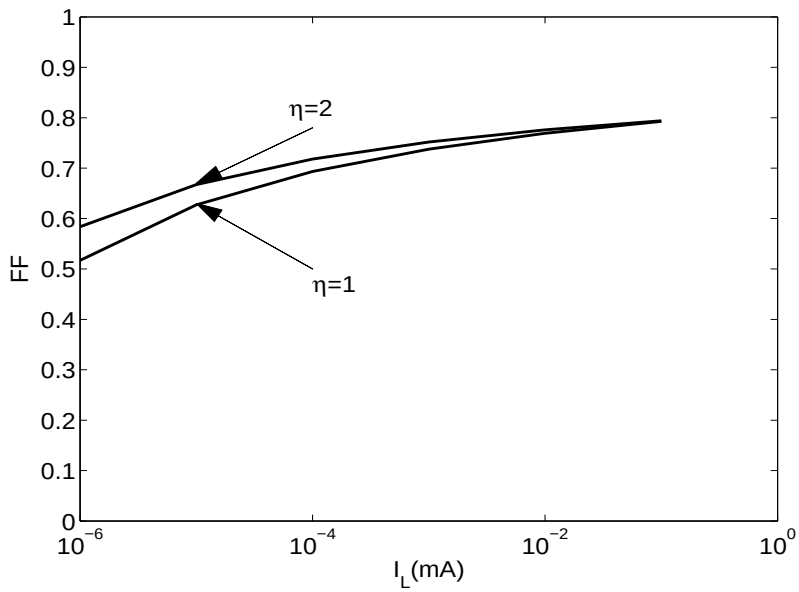

Figure 4.8: The fill-factor as a function of the photocurrent, I_L. Two selections of η are considered. For all cases, I_o is set to 10^{-9} A and the temperature is set to 300 K.

higher fill-factors and therefore greater performance. This result seems counterintuitive. As will be seen later, it arises as an artifact of over simplistic nature by which the recombination processes within a p-n junction have been treated, i.e., through the empirical expression for current, Eq. (4.3), with η set to a value beyond unity, I_o being set at a constant value for all cases. A reanalysis of the role that recombination processes play within p-n junctions, using more a realistic expression for the current-voltage device characteristics, will be presented in Section 4.9. This will show that recombination processes actually reduce the fill-factor. Until that time, the ideality factor, η, is set to unity.

4.6 Relationship with the material properties

Thus far, this analysis has relied upon an empirical model for the current-voltage device characteristic associated with the p-n junction, i.e., Eq. (4.3). Ultimately, of course, these current-voltage device characteristics are related to the underlying material parameters. Drawing upon the insights gleaned from the p-n junction device characteristic determined in Chapter 3, i.e., Eq. (3.40), in the absence of recombination, it can be shown that

$$I = Aq\left[p_{no}\left(\frac{D_h}{\tau_h}\right)^{1/2} + n_{po}\left(\frac{D_e}{\tau_e}\right)^{1/2}\right]\left[\exp\left(\frac{qv}{kT}\right) - 1\right], \qquad (4.7)$$

where A corresponds to the device cross-sectional area, p_{no} is the hole concentration in the n-type region, D_h is the hole diffusion coefficient, L_h is the hole diffusion length, n_p is the electron concentration in the p-type region, τ_e is the electron lifetime, D_e is the electron diffusion coefficient and L_e is the electron diffusion length. Assuming that p_{no} is much greater than n_{po},

i.e., that $p_{no} >> n_{po}$, Eq. (4.7) may be instead expressed as

$$I = Aqp_{no}\left(\frac{D_h}{L_h}\right)^{1/2}\left[\exp\left(\frac{qv}{kT}\right) - 1\right], \tag{4.8}$$

where this expression has been determined using, the relationship between n_i, p_{no}, and p_{po}, i.e., Eq. (3.30). For the material parameters specified in Tables 3.1 and 3.2, it can be shown that for a cross-sectional device area of 1 cm^2, the prefactor, $Aqp_{no}\left(\frac{D_h}{L_h}\right)^{1/2}$, is equal to 10^{-9} A for the case of p_{no} being set to 10^{15} cm^{-3}, this p_{no} selection being representative of that found in a modern photovoltaic solar cell. This value is similar to the nominal selection employed for I_{so}, i.e., 10^{-9} A.

4.7 The role of the parasitic resistances on the performance of a photovoltaic solar cell

In real photovoltaic solar cells, power losses occur owing to the presence of contact resistances at both the front and back contacts of the device and due to current leakage from the edges of the cell. To determine the role that these effects play in shaping the performance of such a solar cell, the approach of Prince is followed [30], and two parasitic resistances are introduced into the model for the p-n junction based on the photovoltaic solar cell: (1) a series resistance, R_s, which acts in series with the parallel combination of the p-n junction and the solar flux controlled current source, this modeling the contact and body resistances associated with the cell, and (2) a shunt resistance, R_{sh}, which acts in parallel to the parallel combination of the p-n junction and the solar flux controlled current source, this modeling

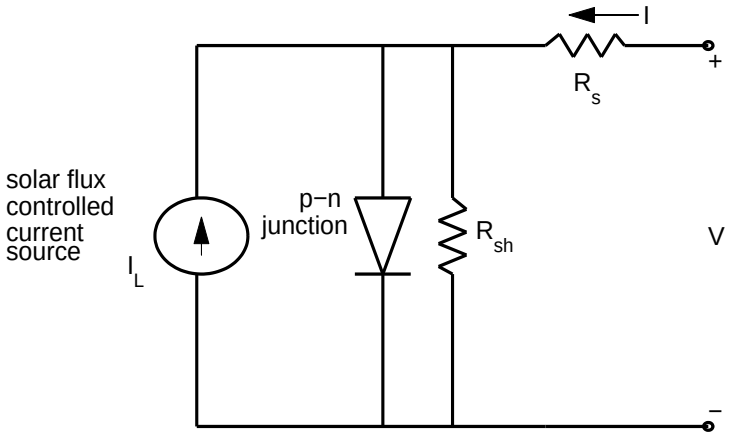

Figure 4.9: The circuit model for a photovoltaic solar cell with the parasitic resistances taken into account.

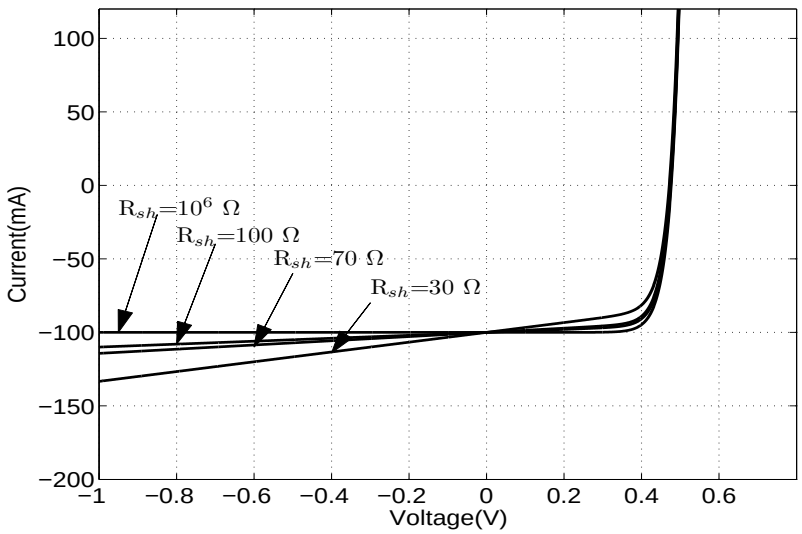

Figure 4.10: The current-voltage device characteristic associated with a photovoltaic solar cell, as modeled in Figure 4.9, for a number of selections of the shunt resistance, R_{sh}. For all cases, I_o is set to 10^{-9} A, I_L is set to 100 mA, and the temperature is set to 300 K. This plot is determined using Eq. (4.9). The series resistance, R_s, is set to zero in all cases.

the current leakage. These resistances are depicted in Figure 4.9. With these resistances taken into account, the resultant current across the contacts to the device may be expressed as

$$I(v) = -I_L + I_o \exp\left(\frac{q(v + IR_s)}{kT}\right) + \frac{v + IR_s}{R_{sh}}, \tag{4.9}$$

where I_0 denotes the scale current, q is the electron charge, k is the Boltzmann constant, T is the temperature, I_L is the photocurrent, R_s is the series resistance, and R_{sh} is the shunt resistance.

The role that the shunt resistance plays in influencing these current-voltage device characteristics is first considered. In Figure 4.10, the current-voltage device characteristics corresponding to a photovoltaic solar cell, as modeled in Figure 4.9, with various selections of the shunt resistance considered, is depicted, the series resistance being set to zero in all cases. For all cases, I_o is set to 10^{-9} A, I_L is set to 100 mA, and the temperature is set to 300 K. It is seen that the shunt resistance, R_{sh}, plays a relatively minor role in shaping the resultant current-voltage device characteristics. As a result, for the purposes of the subsequent analysis, the presence of shunt resistance will be neglected. These values are realistic values corresponding to a modern photovoltaic solar cell.

The role that the series resistance plays in influencing these current-voltage device characteristics is now considered. In Figure 4.11, the current-voltage device characteristics corresponding to a photovoltaic solar cell, as modeled in Figure 4.9, with various selections of the series resistance considered, is depicted, the shunt resistance being set to infinity in all cases. For all cases, I_o is set to 10^{-9} A, I_L is set to 100 mA, and the temperature

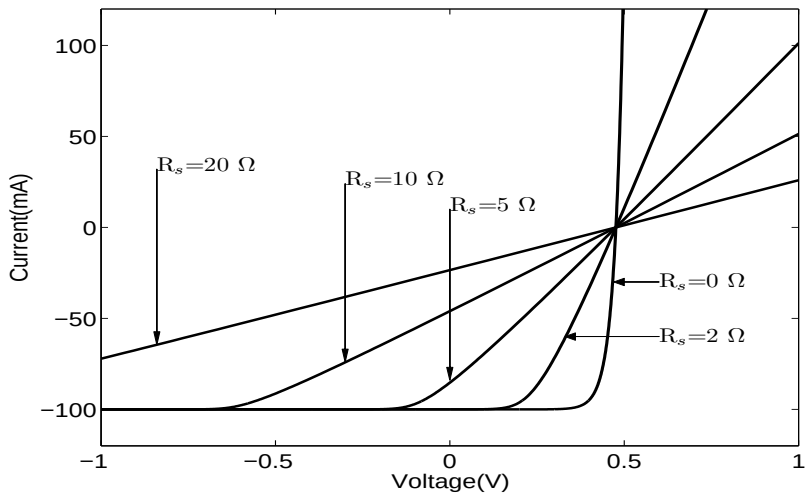

Figure 4.11: The current-voltage device characteristic associated with a photovoltaic solar cell, as modeled in Figure 4.9, for a number of selections of the series resistance, R_s. For all cases, I_o is set to 10^{-9} A, I_L is set to 100 mA, and the temperature is set to 300 K. It is noted that when the current is zero, all the voltages converges on the same point. This plot is determined using Eq. (4.9). The shunt resistance, R_{sh}, is open-circuited in all cases.

is set to 300 K. It is seen that the series resistance, R_s, plays an important role in shaping the current-voltage device characteristics. In particular, it is seen that the current-voltage device characteristic shifts to the left and becomes more sloped with greater series resistance, R_s.

Continuing with the analysis, if the power delivered to an external load, i.e., $p(v) = -I(v)v$, is plotted as a function of the voltage applied across the terminals, then the optimal power may be determined for a number of series resistance selections; see Figure 4.12. As a result, one can determine the fill-factor, FF, as a function of the series resistance, R_s. In Figure 4.13, the obtained fill-factor is plotted as a function of the series resistance, R_s, for the case of I_o set to 10^{-9} A, I_L set to 100 mA, and the temperature set to 300 K. It is seen that the fill-factor dramatically decreases in response to increased R_s. It is interesting to note that at sufficient high R_s, the fill-factor is seen to saturate. Clearly, in photovoltaic solar cell design, minimization of the series resistance is of paramount importance.

4.8 The solar spectrum and photovoltaic solar cell performance

The solar spectra that were introduced in Chapter 2 may now be employed in order to determine the performance of a photovoltaic solar cell. Assuming that each photon with energy in excess of the semiconductor bandgap, E_g, corresponds to a collected charge, the photocurrent may be shown to be

$$I_L = qA\int_{E_g}^{\infty} \frac{S(\omega)}{\hbar\omega} d\omega, \tag{4.10}$$

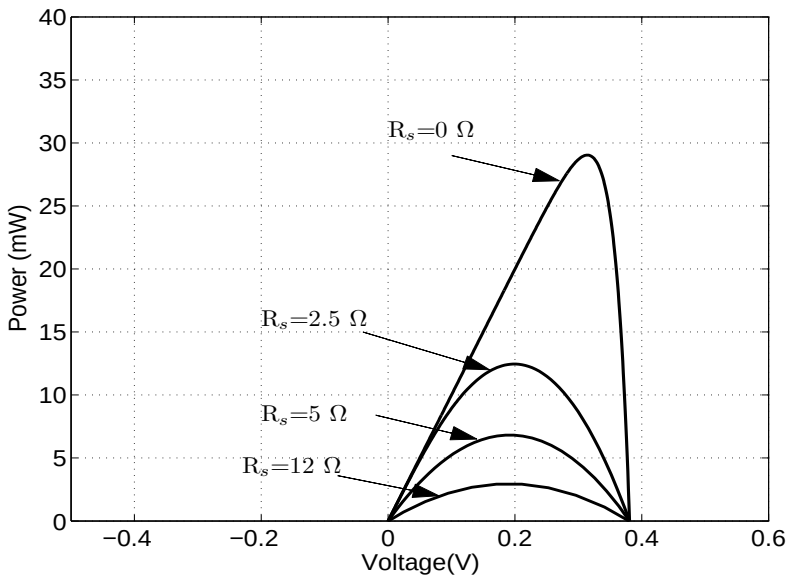

Figure 4.12: The power delivered to an external load as a function of the applied voltage for various selections of R_s. For the purposes of this analysis, I_o set to 10^{-9} A, I_L set to 100 mA, and the temperature set to 300 K.

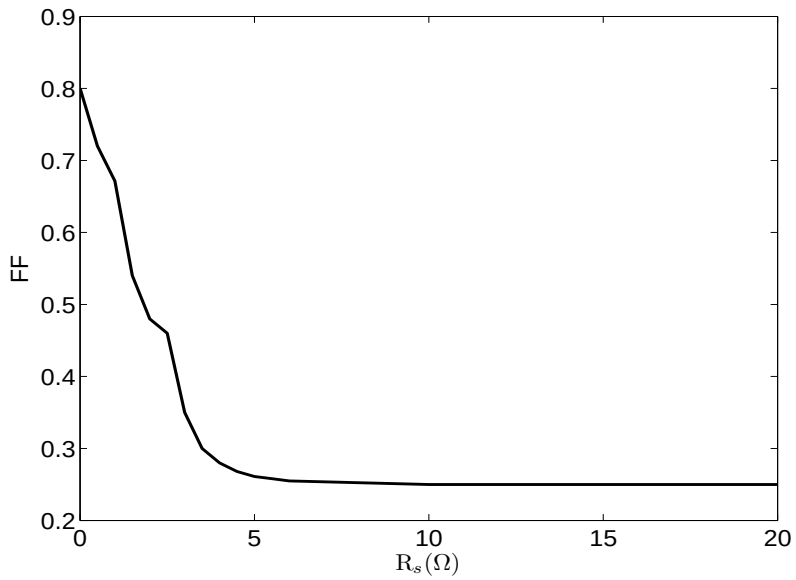

Figure 4.13: The fill-factor, FF, as a function of the series resistance, R_s, for a photovoltaic solar cell, modeled as in Figure 4.9, as a function of the series resistance, R_s. For all cases, I_o is set to 10^{-9} A, I_L is set to 100 mA, and the temperature is set to 300 K.

where $S(\omega)$ denotes the corresponding solar spectrum, $\hbar\omega$ represents the photon energy, q is the electron charge, and A is the cross sectional area of the device. The efficiency of a device provides for the percentage of the solar radiation that may be delivered to the external load. At optimal conditions, this corresponds to

$$\text{efficiency} = \frac{P_{max}}{P_{solar}}, \tag{4.11}$$

where P_{max} corresponds to the maximum power delivered to the load and P_{solar} refers to the overall integrated solar flux received by the solar cell, i.e.,

$$P_{solar} = \int_0^\infty S(\omega)\ d\omega. \tag{4.12}$$

From Eq. (4.1), it is seen that

$$P_{max} = FFI_L V_{oc}, \tag{4.13}$$

where the short-circuit current, I_L, is set to I_{sc}, and V_{oc} may be determined using Eq. (4.4).

The resultant efficiencies are plotted as a function of the energy gap, E_g, in Figure 4.14. This analysis is performed for the AM0 and AM1.5 solar spectra. Results corresponding to the blackbody solar spectrum are also depicted. It is interesting to note that in all cases the efficiency is maximized for energy gaps around 1.5 eV. This is very close to the energy gap corresponding to c-GaAs. As a result, solar cells produced using this material tend to be more efficient than those produced using their c-Si counterparts.

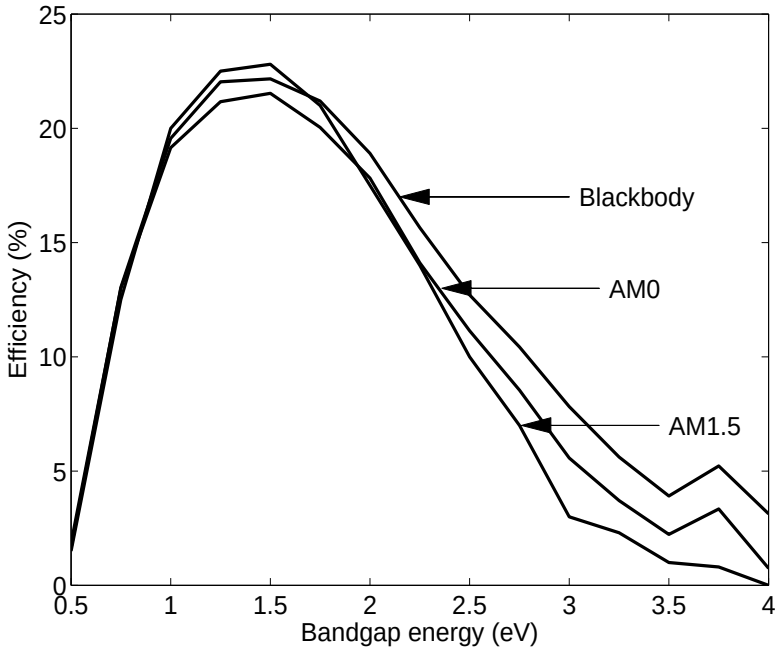

Figure 4.14: The efficiency as a function of energy gap, E_g, for the AM0 and AM1.5 solar spectra. The efficiency corresponding to the blackbody solar spectra is also depicted.

4.9 Recombination within solar cells

As was mentioned previously, the elementary empirical current-voltage device characteristic employed for the purposes of the analysis presented in Section 4.5 leads to erroneous results when the ideality factor is increased beyond unity. In order to assess the true role that recombination processes play in influencing these current-voltage device characteristics, the original equation that was developed in Section 3.7, i.e., Eq. (3.48), will be employed instead for reasonable selections of J_{so} and J_{ro}. For the case of a device with a cross-sectional area, A, set to 1 cm^2, for the selections of J_{so} set to 10 nA/cm^2 and J_{ro} set to 1 μA/cm^2, the current-voltage device characteristic associated with such a p-n junction may be determined. With the solar flux controlled current source added, following the Prince approach [30], the resultant current-voltage device characteristics, neglecting parasitic resistances, may be expressed as

$$I(v) = I_o\left[\exp\left(\frac{qV}{kT}\right) - 1\right] + I_{ro}\left[\exp\left(\frac{qV}{2kT}\right) - 1\right] - I_L, \tag{4.14}$$

where $I_o = AJ_{so}$, $I_{ro} = AJ_{ro}$, and I_L denotes the photocurrent.

This current-voltage device characteristic is plotted as a function of the voltage across the p-n junction device terminals in Figure 4.15, for the case of I_o set to 10^{-9} A, I_{ro} set to 1 μA, I_L set to 100 mA, and the temperature set to 300 K. The power delivered to an external load, $p(v) = -I(v)v$, can be plotted as a function of the voltage using Eq. (4.14), as is seen in Figure 4.16. It is seen that the maximum power delivered to the load, P_{max}, is 30 mW. Thus, the corresponding fill-factor is 0.76, which is noted to be lower than that found for the ideal case; recall, for the ideal case, the fill-factor is 0.7928.

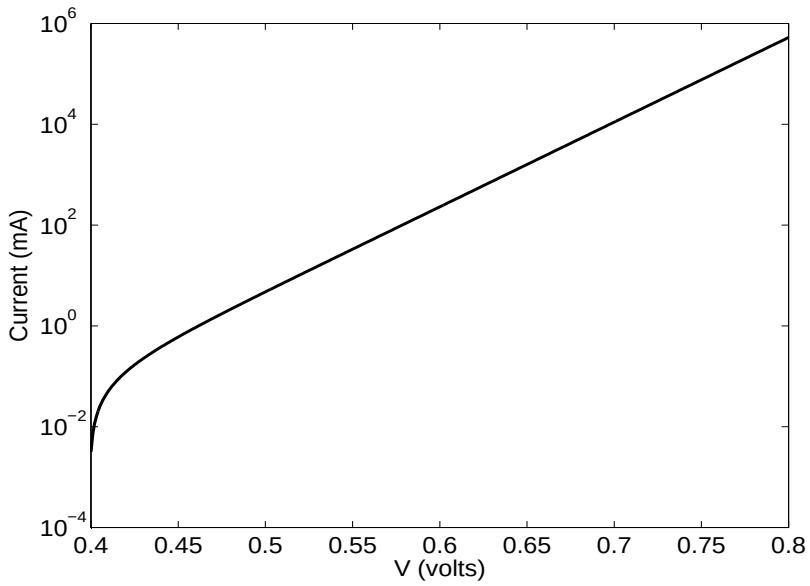

Figure 4.15: This current-voltage device characteristic plotted as a function of the voltage across the p-n junction device terminals. For the purposes of this analysis, I_o is set to 10^{-9} A, I_{ro} is set to 1 μA, I_L is set to 100 mA, and the temperature is set to 300 K.

In Figure 4.17, the fill-factor is plotted as a function of the photocurrent, I_L, for the case of I_o set to 10^{-9} A, I_{ro} set to 1 μA, and the temperature set to 300 K. The result obtained is contrasted with that determined for the ideal case; recall Figure 4.8. It is noted that in all cases, recombination processes reduce the corresponding fill-factor. Thus, the performance is reduced with recombination processes taken into account. This is in accord with experimental observation [15].

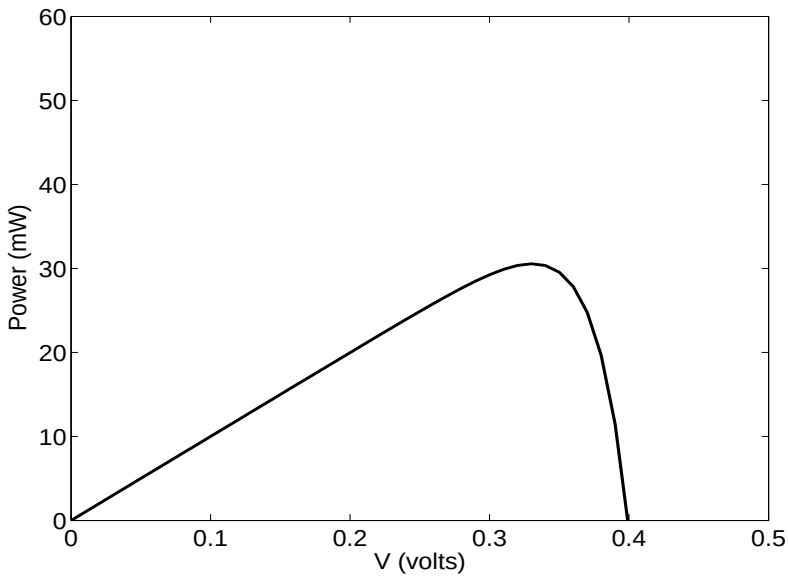

Figure 4.16: The power delivered to the external load as a function of the applied voltage across the terminals of the p-n junction. For all cases, I_o is set to 10^{-9} A, I_{ro} is set to 1 μA, I_L is set to 100 mA, and the temperature is set to 300 K.

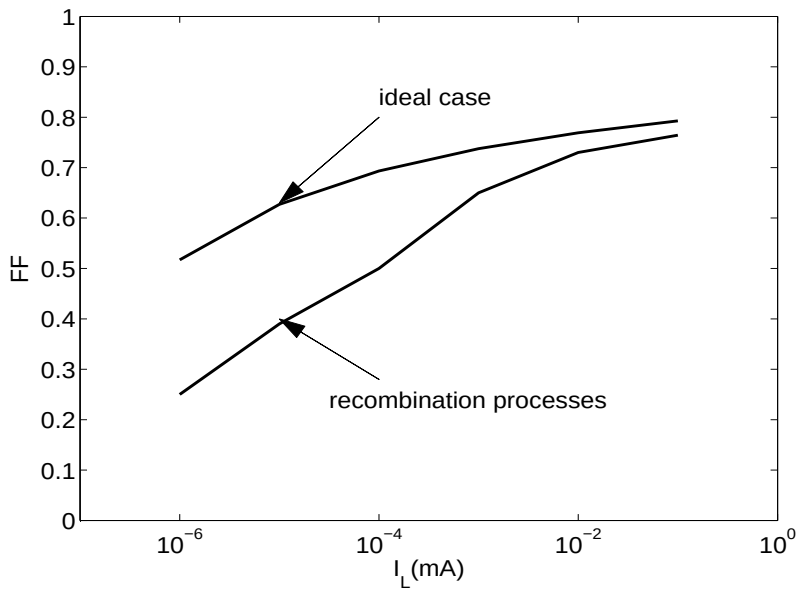

Figure 4.17: Fill-factor as a function of I_L. Both the ideal case and the case with the recombination processes taken into account are considered. For all cases, I_o is set to 10^{-9} A, I_{ro} is set to 1 μA, I_L is set to 100 mA, and the temperature is set to 300 K.

Chapter 5

Conclusions

In conclusion, an elementary model for the analysis of a photovoltaic solar cell has been introduced. This analysis was rooted in the current-voltage device characteristics associated with a p-n junction, in conjunction with a model for the solar flux controlled current source, following the procedure of Prince [30]. Recombination processes were modeled through two means: (1) an empirical expression for the current-voltage device characteristics with an associated ideality factor, η, whose value determines the role of recombination processes, and (2) a more advanced expression that includes a recombination current. It is shown that the simplified, empirical expression is overly simplified and that its use leads to artifacts, i.e., the suggestion that recombination processes could actually increase the fill-factor. In contrast, a more realistic current-voltage device characteristic, i.e., Eq. (4.14), suggests that recombination processes actually reduce the fill-factor. This later observation is in accord with experimental observation.

There are a number of issues that could be further explored. The development of a model, that includes both recombination processes and parasitic resistances, would be useful. The development of a means of extracting the underlying parameter values, from experimental current-voltage device characteristics, would also be useful. Finally, the development of a first principles

analysis, i.e., based on a combination of the charge continuity equation and the ambipolar diffusion equations, would be helpful. These issues will have to be examined in the future.

References

[1] B. A. Osif, *Using the Engineering Literature*, USA: Taylor and Francis, 2006.

[2] A. R. McKirdy, *The Canadian Renewable Energy Guide*, CA: Solar Energy Society of Canada, 1999.

[3] *OECD Economic Surveys: Canada 2008*, Oecd Publishing, vol. 11, 2008.

[4] E. Hau, *Wind Turbines: Fundamentals, Technologies, Application, Economics*, 2nd Ed., Germany: Springer, 2006.

[5] J. E. Welsted, J. C. Everitt, and C. Stadel, *The Geography of Manitoba: its Land and its People*, CA: University of Manitoba Press, 2006.

[6] B. K. Edwards, *The Economics of Hydroelectric Power*, USA: Edward Elgar Publishing Inc., 2003.

[7] Tim Palmer, *Lifelines: The Case for River Conservation*, 2nd Ed., USA: Rowman and Littlefield Publishers Inc., 1994.

[8] P. Gevorkian, *Sustainable Energy Systems Engineering: The Complete Green Building Design*, USA: McGraw-Hill, 2007.

[9] T. L. Baker, *A Field Guide to American Windmills*, Norman: University of Oklahama Press, 1985.

[10] World wind energy association (WWEA), *World Wind Energy Report 2010*, 10th World Wind Energy Conference and Renewable Energy Exhibition, Greening Energy: Converting Deserts into Powerhouses, Egypt: Cario, 2011.

[11] H. H. Schobert, *Energy and Society: An Introduction*, USA: Taylor and Francis, 2002.

[12] K. N. Liou, *An Introduction to Atmospheric Radiation*, International Geophyics series, 2nd Ed., USA: Elsevier Science, vol. 84, 2002.

[13] C. Laughton, *Solar Domestic Water Heating: The Earthscan Expert Handbook for Planning*, UK: Earthscan, 2010.

[14] K. T. Pickering, and L. A. Owen, *An Introduction to Global Environmental Issues*, 2nd Ed., USA: Routledge, 1997.

[15] J. Nelson, *The Physics of Solar Cells*, UK: Imperial College Press, 2003.

[16] A. Luque, and S. Hegedus, *Handbook of Photovoltaic Science and Engineering*, 2nd Ed., UK:John Wiley and Sons, 2011.

[17] R. Hezel, "Progress in manufacturable high-efficient silicon solar cells," *Advanced in Solid State Physics*, vol. 44, pp. 39-49, 2004.

[18] J. Mehra, and H. Rechenberg, *The Historical Development of Quantum Theory*, NY: Springer, 2001.

[19] R. A. Serway, C. J. Moses, and C. A. Moyer, *Modern Physics*, 3rd Ed., USA: Thomos Learning Inc., 2005.

[20] K. Rajagopal, *Engineering Physics*, India: PHI Learing Private Limited, 2008.

[21] J. S. Lewis, *Physics and Chemistry of the Solar System*, 2nd Ed., USA: Elsevier, 2004.

[22] I. N. Mel'nikova, and A. V. Vasilyev, *Short-wave Solar Radiation in the Earth's Atmosphere: Calculation Observation Interpretation*, NY: Springer Berlin Heidelberg, 2005.

[23] F. T. Mackenzie, and A. Lerman, *Carbon in the Geobiosphere: Earth's Outer Shell*, Neitherland: Springer, 2006.

[24] American Society for Testing and Materials (ASTM). (1999, June) Reference Solar Spectral Irradiance: ASTM G-173. [Online]. Available: http://www.rredc.nrel.gov/solar/spectra/am1.5/ASTMG173/ASTMG173.html

[25] C. Tang, R. N. Noyce, and W. Shockely, "Carrier generation and recombination in p-n junction and p-n junction characterstics", Proceeding of the IRE, pp. 1228-1243, 1997.

[26] S. O. Kasap, *Principles of Electronic Materials and Devices*, Boston: Tata McGraw-Hill, 1997.

[27] J. C. Whitaker, *The Electronics Handbook*, USA: Taylor and Francis, 2005.

[28] S. C. Gupta, *Textbook on Optical Fiber Communication and its Applications*, India: Prentice Hall, 2004.

[29] M. C. Jain, *Textbook Of Engineering Physics-Part II*, New Delhi: PHI Learning Private Limited, 2010.

[30] M. B. Prince, "Silicon solar energy converters," *Journal of Applied Physics*, vol. 26, pp. 535-540, 1955.

[31] B. M. Kayes, and H. A. Atwater, "Comparison of the device physics principles of planar and radial p-n junction nanorod solar cells," *Journal of Applied Physics*, vol. 97, pp. (114302)1-11, 2005.